

# The YOPP site Model Intercomparison Project (YOPPsiteMIP) phase 1: project overview and Arctic winter forecast evaluation

5 Jonathan J. Day<sup>1</sup>, Gunilla Svensson<sup>2</sup>, Barbara Casati<sup>3</sup>, Taneil Uttal<sup>4</sup>, Siri-Jodha Khalsa<sup>5</sup>, Eric Bazile<sup>6</sup>, Elena Akish<sup>4</sup>, Niramson Azouz<sup>6</sup>, Lara Ferrighi<sup>7</sup>, Helmut Frank<sup>8</sup>, Michael Gallagher<sup>4,9</sup>, Øystein Godøy<sup>7</sup>, Leslie M. Hartten<sup>4,9</sup>, Laura X. Huang<sup>3</sup>, Gareth Holt<sup>2</sup>, Massimo Di Stefano<sup>7</sup>, Irene Suomi<sup>10</sup>, Zen Mariam<sup>3</sup>, Sara Morris<sup>4</sup>, Ewan O'Connor<sup>10</sup>, Roberta Pirazzini<sup>10</sup>, Teresa Remes<sup>7</sup>, Rostislav Fadeev<sup>11</sup>, Amy Solomon<sup>4,9</sup>, Johanna Tjernström<sup>12</sup>, Mikhail Tolstykh<sup>11,13</sup>,

10 <sup>1</sup>European Centre for Medium-Range Weather Forecasts, Reading, United Kingdom

10 <sup>2</sup>Department of Meteorology and Bolin Centre for Climate Change, Stockholm University, Sweden.

10 <sup>3</sup>Meteorological Research Division, Environment and Climate Change Canada, Canada.

10 <sup>4</sup>NOAA Physical Science Laboratory, Boulder, Colorado, USA.

10 <sup>5</sup>National Snow and Ice Data Center, University of Colorado,

10 <sup>6</sup>Meteo France, Toulouse, France

10 <sup>7</sup>Norwegian Meteorological Institute, Oslo, Norway.

10 <sup>8</sup>Deutscher Wetterdienst, Offenbach, Germany

10 <sup>9</sup>Cooperative Institute for Research in Environmental Science (CIRES), University of Colorado, Boulder, Colorado, USA

10 <sup>10</sup>Finnish Meteorological Institute, Helsinki, Finland.

10 <sup>11</sup>Marchuk Institute of Numerical Mathematics Russian Academy of Sciences, Russia

10 <sup>12</sup>Swedish Meteorological and Hydrological Institute, Linköping, Sweden

10 <sup>13</sup>Hydrometeorological Research Centre of Russia, Russia

Correspondence to: Jonathan J. Day (jonathan.day@ecmwf.int)

## Abstract.

25 Although the quality of weather forecasts in the polar regions is improving, forecast skill there still lags the lower latitudes. So far there have been relatively few efforts to evaluate processes in Numerical Weather Prediction systems using in-situ and remote sensing datasets from meteorological observatories in the terrestrial Arctic and Antarctic, compared to the mid-latitudes. Progress has been limited both by the heterogeneous nature of observatory and forecast data but also by limited availability of the parameters needed to perform process-oriented evaluation in multi-model forecast archives. The YOPP site  
30 Model Inter-comparison Project (YOPPsiteMIP) is addressing this gap by producing Merged Observatory Data Files (MODFs) and Merged Model Data Files (MMDFs), bringing together observations and forecast data at polar meteorological observatories in a format designed to facilitate process-oriented evaluation.

35 An evaluation of forecast performance was performed at seven Arctic sites, focussing on the first YOPP Special Observing Period in the Northern Hemisphere (SOP1), February and March 2018. It demonstrated that although the characteristics of forecast skill vary between the different sites and systems, an underestimation in boundary layer temperature variability across  
models, which goes hand in hand with an inability to capture cold extremes, is a common issue at several sites. Diagnostic analysis using surface fluxes suggests that this is at least partly related to insufficient thermal representation of the land-surface in the models, which all use a single layer snow model.

Deleted: nce

## 40 1 Introduction

Recent decades have seen a marked increase in human activity in the polar regions leading to an increasing societal demand for weather and environmental forecasts (Emmerson and Lahn, 2012; Goessling et al., 2016). Despite this growing need, the skill of weather forecasts in the polar regions lags that of the mid-latitudes (Jung et al., 2016; Bauer et al., 2016). This is partly the result of the relatively lower density of conventional observations in high compared to mid-latitudes (Lawrence et al.,

2019), but is also related to the occurrence of meteorological situations and phenomena which are historically difficult to model such as stable boundary layers (e.g. Atlaskin and Vihma, 2012; Sandu et al., 2013; Holtslag et al., 2013), mixed-phase clouds (e.g. Pithan et al., 2014, 2016, Solomon et al., 2023), and the importance of coupling between the atmosphere and snow and ice surfaces (e.g. Day et al., 2020; Batrak and Müller, 2019; Svensson and Karlsson, 2011).

50

The ability of climate models to represent atmospheric processes in polar regions has recently been assessed highlighting deficiencies in near-surface and boundary layer properties (Pithan et al., 2014; Svensson and Karlsson, 2011; Karlsson and Svensson, 2013). Since many climate models are based on global weather forecasting systems, understanding the causes of forecast error after 1-2 days may help develop understanding of the sources of error in climate models (Rodwell and Palmer, 55 2007). Nevertheless, until recently there has been little focus on evaluating Numerical Weather Prediction (NWP) models using in-situ data from the terrestrial Arctic and Antarctic (Jung and Matsueda, 2016; Jung et al., 2016).

**Deleted:** 4

Recent studies, conducted as part of the World Weather Research Programme's Polar Prediction Project (PPP, Jung et al., 60 2016) have started to address this gap, assessing the skill of both the large scale circulation (Bauer et al., 2016) and surface weather properties (Køltzow et al., 2019). The Year of Polar Prediction (YOPP) site Model Intercomparison Project (YOPPsiteMIP) was designed to build on these earlier studies by utilising process level data from polar observatories to 65 diagnose the causes of forecast error from a process perspective and ultimately inform model development. Although process-oriented evaluation studies focussing on polar processes are not new, those that have been done have tended to focus on one or two sites or a specific field campaign (see Day et al., 2020; Batrak and Müller, 2019; Miller et al., 2018; Tjernström et al., 2021, Kähnert et al., 2023 for some recent examples). A key aim of YOPPsiteMIP is to provide a pan-Polar perspective on forecast evaluation and process representation.

YOPPsiteMIP participants were asked to provide data in so-called Merged Data Files (MDFs) which includes both Merged Observatory Data Files (MODFs), for observatory data, and Merged Model Data Files (MMDFs), for model data. These data 70 standards, which were developed specifically for YOPPsiteMIP, are described by Uttal et al. (2023). Using this common file format, with consistent naming and metadata, facilitates equitable and efficient comparisons between models and observations. This standardisation of the data from different observatories also aids interoperability in the sense that the same evaluation code can be applied at different sites. These MDF filetypes were developed as part of PPP, following the FAIR (Findable, Accessible, Interoperable, Reusable) data principles (Wilkinson, 2016). Details of the MDF concept and specifics of the data 75 processing chain for producing MDFs are described in Uttal et al. (2023).

**Deleted:** and related Python toolkit

**Deleted:** and Gallagher et al., (in prep).

The observatories selected for YOPPsiteMIP represent a geographically diverse set of locations (see Mariani et al. 2024). At 80 these sites a wide range of instruments measuring properties of the air, snow and soil are employed, extending far beyond the traditional synoptic surface and upper-air observation network, which are collected for use in the production and evaluation of NWP systems (Uttal et al., 2015). Taken together, the observations collected at these observatories offer opportunities to develop a deeper understanding of the physical processes governing the weather in the polar regions, their representation in forecast models, and how this varies from site to site. The processes and phenomena targeted in YOPPsiteMIP include boundary-layer turbulence, surface exchange (including over snow and ice) and mixed-phase clouds.

85 A benefit of organizing coordinated evaluation involving several NWP systems and multiple sites is that it helps clarify if the issues revealed by the analysis are model or location specific. The modelling community has organized model inter-comparisons to target various atmospheric processes relevant for Arctic conditions (e.g. Cuxart et al., 2006; Pithan et al., 2016; Tjernström et al 2005, Sedlar et al. 2020, Solomon et al., 2023) each using its own protocol for data sharing. However, the

newly developed standardisation of the observational and forecast model data developed for YOPPsiteMIP is planned to be used for future MIIPs (model intercomparison and improvement projects). Converging on a standard like this will aid interoperability, making it easier for model developers to expand their evaluation to new sites or observational campaigns, but also to other models or forecasting systems.

95

MDFs were requested for the locations listed in Table 1 and shown in Figure 1 during the YOPP Special Observing Periods, during which the observations taken at many polar observatories (e.g. the frequency of radiosondes) was enhanced (see Lawrence et al., 2019; Bromwich et al., 2020). For the Northern Hemisphere the periods Feb–Mar 2018 and Jul–Sep 2018 were selected and named NH-SOP1 and SOP2 respectively. For the Southern Hemisphere or SH-SOP the period Nov–Feb 2018/19 was chosen. At the time of publication MMDFs have been produced and archived from seven NWP systems for these periods and all of the sites listed have MMDFs from at least one model. MODFs have been produced and archived for seven of the sites so far and it is hoped that additional MODFs will be produced in the future to fill the gaps, particularly in the Southern Hemisphere.

100

105

**Deleted: M**

Observatory name Filename	Latitude Longitude	Elevation
------------------------------	--------------------	-----------

#### Arctic land sites

Utqiāgvik (Formerly known as Barrow, Alaska) <i>Utqiagvik</i>	71.32°N, 156.62°W	8-20 m
Oliktok Point (Alaska) <i>oliktok</i>	70.50°N 149.89°W	2-6 m
Whitehorse (Canada) <i>whitehorse</i>	60.71°N, 135.07°W	682 m
Eureka (Canada) <i>eureka</i>	80.08°N 86.42°W	0-610 m
Iqaluit (Canada) <i>iqaluit</i>	63.74°N, 68.51°W	5-11 m
Alert (Canada) <i>alert</i>	82.49°N, 62.51°W	8-210 m
Summit (Greenland) <i>summit</i>	72.58°N, 38.48°W	3210-3250 m
Ny-Ålesund (Svalbard) (Zeppelin station) <i>nyalesund</i>	78.92°N, 11.53°E (78.9°N, 11.88°E)	0-30 m (473 m)
Sodankylä (Finland) <i>Sodankylä</i>	67.37°N, 26.63°E	198 m
Pallas (Finland) <i>pallas</i>	67.97°N, 24.12°E	305 m

Tiksi (Russia) <i>tiksi</i>	71.60°N, 128.89°E	1-30 m
Cherskii (Russia) <i>cherskii</i>	68.73°N, 161.38°E (68.51°N, 161.53°E)	8 m (16 m)
Ice Base Cape Baranova (Russia) <i>baranova</i>	79.3°N, 101.7°E	24 m

#### Arctic Ocean sites

SHEBA location <i>sheba</i>	165°W, 76°N	Sea level
Arctic Ocean 1 (Gakkel Ridge) <i>aol</i>	10°E, 85°N	Sea level
Arctic Ocean 2 (North Pole) <i>ao2</i>	0°E, 90°N	Sea level
Arctic Ocean 3 (Canada Basin) <i>ao3</i>	135°W, 81°N	Sea level

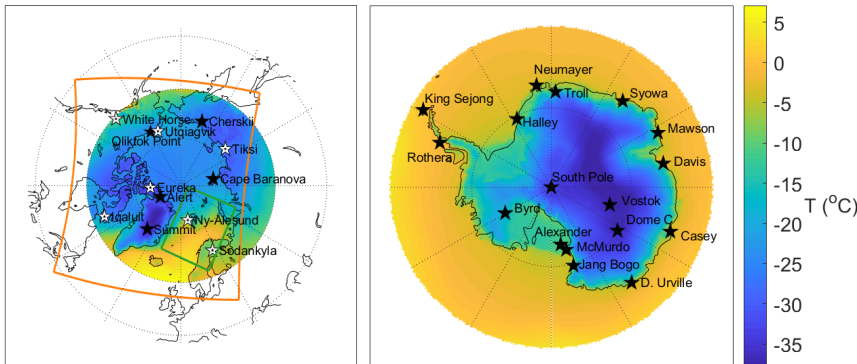
#### Antarctic land sites

Alexander Tall Tower <i>alexander</i>	79.01°S, 170.72°E	55 m
Casey <i>casey</i>	66.28°S, 110.53°E	30 m
Davis <i>davis</i>	68.58°S, 77.97°E	
Dome C <i>domec</i>	75.08°S, 123.34°E	3233 m
Dumont d'Urville <i>dumont</i>	66.66°S, 140.01°E	0-50 m
Halley IV <i>halley</i>	75.58°S, 26.66° W	130 m
King Sejong (King George Island) <i>kingsejong</i>	62.22°S, 58.79° W	10 m

Georg von Neumayer <i>neumayer</i>	70.65°S, 8.25°W	42 m
Mawson <i>mawson</i>	67.60°S, 62.87°E	15 m
Syowa (Showa) <i>syowa</i>	69.00°S, 39.59°E	18-29 m
Jang Bogo (Terra Nova Bay) <i>jangbogo</i>	74.62°S, 164.23°E	36 m
Amundsen-Scott South Pole <i>southpole</i>	90°S, 0°E	2835 m
Byrd <i>byrd</i>	80.01°S, 119.44°W	1539 m
Rothera <i>rothera</i>	67.57°S, 68.13° W	4 m
Vostok <i>vostok</i>	78.46°S, 106.84°E	3489 m
McMurdo (Scott base) <i>mcmurdo</i>	77.85°S, 166.67°E (77.85°S, 166.76°E)	10 m (10 m)
Troll <i>troll</i>	72.01°S, 2.54°E	1275 m

Table 1: List of YOPPsiteMIP observatory locations: name, *name as used in filenames*, latitude, longitude and elevation.

Where an elevation range is stated, this is because the instruments at a given observatory extend over a range of values due to variations in local topography.



115 **Figure 1:** Maps of the ERA5 2m-temperature climatology (1990-2019) for February-March (time of NH-SOP1) for Arctic (left) and for November-February (SH-SOP) for Antarctic (right). The observatories used in YOPPsiteMIP are marked with stars. White stars indicate the sites where MODFs are currently available, which are the subject of this study; black stars indicate the sites whose MODFs are not yet complete. The orange and green boxes depict the extent of the ECCC-CAPS and AROME-Arctic domains respectively.

120 The purpose of this paper is two-fold: firstly, to document the first version of the YOPPsiteMIP dataset along with a basic description of the forecasting systems and their respective MMDFs that are archived at the YOPP Data Portal, hosted by the Norwegian Meteorological Institute (MET Norway). Secondly, the paper presents a multi-site evaluation of seven forecasting systems during NH-SOP1, at seven Arctic observatories that have produced MODFs. The locations are indicated by the white stars in Figure 1a and the MODFs and [full](#) details of the sites are described in [Mariani et al., \(2024\)](#).

125 The seven Arctic sites used for evaluation in this study cover both high and sub-Arctic climate zones. Tiksi, Utqiagvik, Iqaluit, Ny-Ålesund and Eureka all sit in the Arctic tundra characterised by low vegetation. The remaining two sites Whitehorse and Sodankylä are sub-Arctic, with higher vegetation corresponding to the boreal cordillera and taiga ecozones respectively. Whitehorse, Iqaluit, Ny-Ålesund and Eureka are characterised by complex topography in the surrounding area, whereas the other sites are flatter. All the sites are in close vicinity to either frozen ocean (sea ice) or frozen inland water bodies at this time of year and the land surrounding each observatory is covered in snow throughout the period Feb-Mar 2018. A visual representation of the model grids with respect to the landscape surrounding these stations can be seen in Fig 2 of Mariani et al., (2024) in which a more detailed description of the site characteristics may be found.

**Deleted:** Morris

**Deleted:** in prep

**Deleted:** low

## 2 Description of simulations, model formulation and output protocol

135 To date, six NWP centres have submitted forecasts from seven forecasting systems for SOP1 & SOP2, with two systems submitted for the SH-SOP (see Table 2). Four of the systems are global:

- The Integrated Forecasting System from the European Centre for Medium-Range Weather Forecasts (ECMWF-IFS; Day et al., 2023),
- The Action de Recherche Petite Echelle Grande Echelle from Meteo France (ARPEGE-MF ; Bazile and Azouz, 2023a),
- The Semi-Lagrangian, based on the absolute vorticity equation from the Hydrometeorological Research Centre of Russia (SLAV-RHMC, Tolstykh, 2023) and,
- The Icosahedral Nonhydrostatic Model from Deutscher Wetterdienst (DWD-ICON; Frank, 2023).

140 Three are regional:

- The Canadian Arctic Prediction System from Environment and Climate Change Canada (ECCC-CAPS; Casati, 2023)

150 • and two versions of Applications of Research to Operations at Mesoscale (AROME) from Meteo France (AROME-MF; Bazile and Azouz, 2023b) and from MET Norway (AROME-Arctic; Remes, 2023).

The domain boundaries of the regional forecasting systems can be seen in Figure 1 (note that only two of the observatories are within the AROME domain). The forecasts analysed here were initialised at 00 UTC for each day of the SOPs (although 12UTC forecasts are also available on the archive for many of the systems). The forecast leadtime varies between the different systems but all forecasts are at least two days long (see Table 2 and Figs 2 & 3).

155

The files for some of the systems (CAPS, SLAV, ARPEGE, AROME-MF) are provided with multiple grid-points, centred on the observatory location. For others only a single grid-point was provided. Multiple grid-points centred around the observatory location were requested because many of the observatories are located in the vicinity of coasts, which leads to representativeness issues when comparing the land-based observation to model output for grid-points being partially or entirely over the ocean. In this study when there are multiple grid points we choose the closest 100% land point to the supersite location, with the exception of CAPS, for which the central grid-point within a beam of 7x7 grid-points was considered (since nearest to the observation site) and ICON which provided the single closest gridpoint to the station location. As a result, the evaluation utilises a 100% land gridbox at all models and locations, with the exception of ICON, which has 23% land cover at the Utqiagvik and 73% at Ny-Ålesund, and CAPS, which has 37% land cover in Utqiagvik, 71% and 77% in Tiksi and Iqaluit, and over 90% land cover for the other sites. Comparison of the CAPS grid-points surrounding Utqiagvik with each other indicated that the evaluation would not be much influenced by the choice of gridcell (not shown), since during the Arctic winter the frozen ocean gridpoints have similar properties to the snow-covered land surface (e.g. when analysing the surface energy budget sensitivity to radiative forcing in Section 3.4). The grid resolutions range from 2.5 km to ~30 km and the model timestep varies from 1.5 to 7.5 min (see Table 2).

160

165 The models have quite a diverse mixture of formulations for atmospheric dynamics, land surface, sub-grid scale parameterisations and initialisation/data assimilation procedures. More details about the simulations with specific models are provided below and a summary of the key model components/parameterisations used in each model is included in Table 3.

170

175 2.1 IFS-ECMWF  
MMDFs for the operational forecasts with the IFS high resolution deterministic forecasts are available for the period starting Jan 2018. The initial forecasts are produced with IFS cycle 43r3 which was an atmosphere only model with persisted sea ice and anomaly SSTs. From 5 June 2018 (i.e. before SOP2) the forecasts were produced with cycle 45r1 which included dynamic sea ice and ocean fields (see Day et al., 2022 for more information). Although the model version changes the horizontal (~9km) and vertical resolution (L137) are the same in all SOPs. The data archived in the MMDFs is provided at the model timestep (7.5 min) for a single model grid point closest to the observatory. In addition to the grid point data a number of parameters (including albedo, surface temperature and surface energy fluxes) are provided on the land-surface model tiles to enable detailed evaluation of processes even at heterogeneous sites. A complete description for the two versions of the IFS can be found here: <https://www.ecmwf.int/en/publications/ifs-documentation>.

180

185 2.2 ARPEGE-MF  
The version of ARPEGE submitted to YOPPsiteMIP was a pre-operational version based on the cy43t2\_op1 operational system but coupled with the 1D sea-ice model GELATO (Bazile et al. 2020). The resolution of the model used for these simulations is the same as is used operationally at Meteo France which is variable (using a stretching factor of 2.2) with the pole (highest resolution of 7.5 km) over France for SOP1 and SOP2 and over Antarctica in SOP-SH and 105 vertical levels. The horizontal resolution is about 8-9 km over the North-Pole and timeseries have been provided for the three SOPs in the

**Deleted:** on  
**Deleted:** and there are issues with  
**Deleted:** , over land or blended

**Deleted:** .38  
**Deleted:** 0.69  
**Deleted:** .17  
**Deleted:** While we expected land-processes in  
**Deleted:** to be mis-represented by  
**Deleted:** these CAPS  
**Deleted:** and ICON  
**Deleted:** ocean-dominated grid-points  
**Deleted:** .  
**Deleted:** this revealed  
**Deleted:**  
**Deleted:**  
**Deleted:** not always  
**Deleted:** to  
**Deleted:** be the case,  
**Deleted:** acts as  
**Deleted:** .  
**Deleted:**  
**Deleted:**

MMDF format for the 21 YOPP observatories with an hourly output for both state variables (instantaneous) and fluxes  
215 (accumulated).

### 2.3 SLAV-HMRC

MMDFs were produced by the SLAV model (Tolstykh et al., 2018) for both SOP1 and SOP2 containing 7-day forecasts starting at 00 UTC. The output is available for 4 horizontal grid points surrounding selected observatories, every 15 minutes  
220 (i.e. every fourth timestep). Depending on variable, the output is instantaneous or a 15-min averaged value. Data for 13 of the Arctic observatories in Table 1 are provided. Selection of observatories is based on model resolution in latitude which is relatively low, ~16 km in Northern polar areas; also, the ao2 point is not included because the model grid does not contain the poles.

**Deleted:** y

### 2.4 ICON-DWD

MMDFs from DWD's ICON (Zängl et al., 2015) are available from February 2018 to June 2020 containing 7.5-day forecasts starting at 00 and 12 UTC for Sodankylä, Ny-Ålesund, and Utqiagvik (Barrow). The mesh width is 13 km. Different model versions are used during this period. In February icon-nwp-2.1.02 was used followed by icon-2.3.0-nwp0 during 2018-02-14 to 2018-06-06, and from 2018-09-19 to 2018-12-05 icon-2.3.0-nwp2 was in operation. Since 2018-02-14, a new orographic  
230 data set came in operations, however, for the 3 data points provided the changes were less than 1 m in height. The sea ice analysis used in ICON, was based on the Real-Time Global SST High Resolution Analysis of NCEP until 2018-07-16. Since then it is based on the Operational Sea Surface Temperature and Sea Ice Analysis (OSTIA; Donlon et al., 2012). To represent variations of subgrid scale surface characteristics ICON uses a tile approach. Since 2018-07-16 the tile values of surface fluxes, and other tile dependent variables are included in the MMDFs in addition to the grid average values. Hourly output is available  
235 based on a timestep of 120s.

**Deleted:** 2

### 2.5 CAPS-ECCC

MMDFs for ECCC-CAPS are available for the whole period from February 2018 to December 2018. Prior to the 28th of June 2018 CAPS was uncoupled and run with the GEM version 4.9.2. After the 29th of June 2018 CAPS was coupled with the  
240 Regional Ice and Ocean Prediction system (RIOPS) and run with the GEM version 4.9.4. Atmospheric Lateral Boundary Conditions (LBCs) and initial conditions (ICs) are from ECCC Global Deterministic Prediction System (GDPS). Initial surface fields are from the Canadian Land Data Assimilation System (CaLDAS). The CAPS timeseries are produced for a beam of 7 x 7 grid-points centred on each of the twelve land-based Arctic observatories listed in Table 1. Timeseries up to 48 hours leadtime are made available for the daily runs initialized at 00 UTC. The data is archived with a time frequency of 7.5 min,  
245 equivalent to five timesteps of 90 s each.

### 2.6 AROME-ARCTIC

MET Norway utilises the HARMONIE-AROME (HIRLAM-ALADIN Research on Mesoscale Operational NWP in  
250 Euromed—Application of Research to Operations at Mesoscale) model configuration (Bengtsson et al., 2017) for operational weather forecasting for the European Arctic with the name AROME-Arctic (Muller et al., 2017). AROME-Arctic MMDFs are based on the operational forecasts (cy40h.1) and are available for the SOP1 and SOP2 at Sodankylä and Ny-Ålesund. LBCs are derived from the ECMWF IFS-HRES described in Section 2.1. Assimilation of conventional and satellite observation with 3DVAR in the upper atmosphere, optimal interpolation of snow depth, screen level temperature and relative humidity in the surface model. Temperature tolerance in the surface assimilation scheme was increased on 15 March 2018 to better assimilate  
255 observed low temperatures. The data archived in the MMDFs are provided hourly for the single model grid-point closest to the site. Model data for the full domain in its original format are also available via thredds.met.no.

## 260 2.7 AROME-MF

The AROME -MF system from Météo-France and AROME-ARCTIC from MET Norway are both configurations of the same model system but use different parameterizations of turbulence, shallow convection, cloud microphysics and sea ice. The system used for the YOPPSiteMIP differs from the operational AROME-France configuration (Seity et al., 2011) and the version evaluated for SOP1 in Kołtzw et al., (2019) in that it is coupled with the GELATO 1D sea ice model. However, the 265 domain (see Figure 1a), horizontal and vertical grid are exactly the same as the AROME-ARCTIC operational system (see Section 2.6). The ICs and LBCs are interpolated from the global model ARPEGE-MF simulation described above (Section 2.2). The MMDF files have been produced for Ny-Ålesund, Sodankylä and Pallas with hourly output.

## 270 2.8 Output format

For each forecast initial time and each forecasting system a single netCDF file containing all variables was archived following the MMDF format, which use the same nomenclature, metadata, and structure as the MODFs. In order to be able to assess process representation, the YOPPSiteMIP protocol requested that atmospheric fields were provided on native model vertical levels and all fields should be provided with high frequency (every 5 or 15 minutes), ideally at the frequency of the model timestep if practical [to support detailed process investigations without the confounding effect of time averaging](#).

275 The actual variables archived, frequency and number of grid-points, vary from model to model. For example, ECCC provided a comprehensive set of parameters for the CAPS model focusing on precipitation and clouds microphysics to allow studies on the representation of different types of hydrometeors by the P3 scheme (Morrison and Milbrandt, 2015; Morrison et al., 2015; Milbrandt and Morrison, 2016). A full list of requested variables, along with a schema for producing the MDFs are described 280 in a document known as the H-K Table (Hartten and Khalsa, 2022). The table is available in both human and machine-readable form (PDF and JSON, respectively). The H-K Table relies on standards and conventions commonly used in the earth sciences, including netCDF encoding with CF naming and formatting conventions and is an evolving document that is expected to evolve to fulfil the requirements of future MMDFs and MODFs. The prescribed metadata make data provenance clear and encourage proper attribution of data origin (see further information in Uttal et al., 2023).

**Deleted:** (Gallagher et al., in prep.)

285 Although we only focus on model performance during SOP1, a full set of MMDFs and MODFs was produced for both SOPs. The MODFs for Iqaluit (Huang et al., 2023a), Whitehorse (Huang et al., 2023b), Utqiāġvik (formerly known as Barrow: Akish and Morris, 2023<sup>a</sup>), Eureka (Akish and Morris, 2023<sup>a</sup>), Tiksi (Akish and Morris, 2023<sup>b</sup>), Ny-Ålesund (Holt, 2023) and 290 Sodankylä (O'Conner 2023) are described in detail in [Mariani et al., \(2024\)](#) along with descriptions of the site geography. MMDFs have also been produced for the SH-SOP with the ECMWF-IFS and ARPEGE models (See Table 2), but no MODFs for the Antarctic observatories have been produced yet.

**Deleted:** a  
**Deleted:** b  
**Deleted:** c  
**Deleted:** Morris  
**Deleted:** 3  
**Deleted:** y

Centre	Model-name	Global/Regional and horizontal/vertical resolution	<a href="#">Dynamics</a> , timestep/output frequency/forecast length	Version	Key Reference(s)	SOPs in YOPP portal
--------	------------	----------------------------------------------------	----------------------------------------------------------------------	---------	------------------	---------------------

**Deleted:** Physics

ECMWF	IFS	Global: 9km/L137	7.5min/7.5min/3d	Cy43r3 for SOP1, Cy45r1 for SOP2 & SOP-SH	Buizza et al., (2017)	SOP1, SOP2 & SOP-SH
Meteo-France	ARPEGE-MF <sub>w</sub>	Global: 7.5-25km/L105	240s/60min/4d	cy43t2_op2	Pailleux et al. (2014)	SOP1, SOP2 & SOP-SH
Meteo-France	AROME-Arctic	Regional: 2.5km/L65	50s/60min/2d	cy43t2_op2	Seity et al., (2011)	SOP1 & SOP2
ECCC	CAPS	Regional: 3km/L62	1.5min/7.5min/2d	vn1.0.0 for SOP1 & vn1.1.0 for SOP2	Milbrandt et al., (2016) Casati, et al., (2023)	SOP1 & SOP2
DWD	ICON	Global: ~13km/L90	2min/60min/7.5d	icon-nwp-2.1.02, icon-2.20-nwp0, icon-2.30-nwp0, icon-2.30.nwp2	Zängl et al., (2015) Prill et al., (2020)	SOP1 & SOP2
HMCR	SLAV	Global: ~20km/L51	3.75min/15min/3d	SLAV20 (2018)	Tolstykh et al., (2018) Tolstykh et al., (2017)	SOP1 & SOP2
MET Norway	AROME-Arctic	Regional: 2.5km/L65	50s/60/2d	HARMONIE-AROME cy40h	Müller et al. (2017) Bengtsson et al., (2017)	SOP1 & SOP2

**Deleted: GELATO**

**Table 2. Summary of forecasting systems**

Model-name	Land-surface model	Surface layer/Fluxes	Turbulent diffusion	Orographic drag	Convection	Cloud microphysics	Radiation	Dynamical core
IFS	HTESEL: Balsamo et al., (2009)	K-diffusion with stability functions of Dyer (1974) and Höglström (1988) and Holtslag and De Bruin (1988) in unstable conditions and for stable conditions	EDMF Köhler et al., (2011) in unstable conditions and K-diffusion (Louis, 1979; Sandu et al., 2013) in stable conditions	Following Lott and Miller (1997) and Baines and Palmer (1990)	mass-flux for deep, shallow and mid-level convection: Tiedtke (1993) and Bechtold et al. (2008)	double moment scheme with four categories of hydrometeor	EcRad (Hogan and Bozzo, 2018) Is based on the Rapid Radiation Transfer Model (RRTM, Mlawer et al., 1997; Iacono et al., 2008)	Spectral/FE/H
ARPEGE	SURFEX: Masson et al., (2013)	K-diffusion with modified version of Louis (1979)	TKE: Cuxart et al., (2000) with a modified mixing length (Bazile et 2011)	Scheme described in Cuxart et al., (2008) following Lott et al., (2008) following Bougeault (1985) and and Miller (1997) for mass flux for shallow gravity wave drag, and an envelope approach (after Wallace et al., 1983)	Mass flux for deep convection following Bougeault (1985) and gravity wave drag, and an orography approach (after Wallace et al., 1983)	Single moment with five categories of hydrometeor (Seity et al., 2012)	RRTM	Spectral/FE/H <b>Deleted: i</b>
AROME-MF	SURFEX: Masson et al., (2013)	K-diffusion with stability function of Louis (1979)	TKE: Cuxart et al., (2000)	N/A	Deep convection is explicitly represented and shallow uses the Pergaud et al. (2009) EDMF scheme.	Single moment with six categories of hydrometeor (ICE3; Pinty and Jabouille 1998)	RRTM	Spectral/FD/NH
CAPS	ISBA: Noilhan and Planton (1989) and Bélair et al. (2003)	K-diffusion with stability functions of Delage and Girard (1992) in unstable conditions and Delage (1997) in stable conditions.	TKE with statistical representation of subgrid-scale cloudiness (MoisTKE: Bélair et al. (2005))	Lott and Miller (1997)	Deep convection from the Kain and Fritsch (1990) mass flux scheme and shallow convection from a Kuo-transient scheme (Bélair et al., 2005)	Double moment with Predicted Particle Properties (P3; Morrison and Milbrandt, 2015; Morrison et al., 2015; Milbrandt and Morrison, 2016)	Correlated-k distribution radiative transfer scheme (Li and Barker, 2005)	Gridpoint/FE (horizontal)&FD(vertical)/NH (Coté et al. 1998a,b; Girard et al, 2014)

ICON	TERRA: Heise et al., (2006)	transfer-resistances approach: Baldauf et al., (2011)	TKE Baldauf et al., (2011) and Raschendorfer (2001)	Lott and Miller (1997)	mass-flux for deep, shallow and mid-level convection: Tiedtke (1993) and Bechtold et al. (2008)	Single moment scheme with four hydrometeors (Seifert, 2008)	RRTM	Grid-point/FV/NH
SLAV	ISBA 2L: Noilhan and Planton (1989) with modifications	Stability functions based on Cheng et al. (2002) with modifications leading to the absence of critical gradient Richardson number in the system.	TOUCANS (TKE+TTE) <a href="#">(Bašták-Ďurán et al 2014)</a>	Scheme described in Catry et al., (2008) following Lott <a href="#">(Bašták-Ďurán et al 2014)</a> and Miller (1997) for according to gravity wave drag, and an envelope orography approach (after Wallace et al., 1983)	Mass flux following Bougeault (1982) but with modifications and Miller (1997) for according to gravity wave drag, and an envelope orography approach (after Wallace et al., 1983)	Single moment scheme with four hydrometeors (Gerard et al., 2009)	Shortwave radiative transfer uses the CLIRAD model (Tarasov and Fomin, 2007) and RRTM for longwave	Grid-point/FD/H Tolstykh et al., (2017)
AROME-Arctic	SURFEX: Masson et al. (2013)	Based on Louis (1979)	HARATU: TKE together with a diagnostic length scale  (Lenderink and Holtslag 2004; van Meijgaard et al. 2012)	N/A	Deep convection is explicitly represented and Shallow is represented by EDMF (Soares et al. 2004; Siebesma et al. 2007, Bentsson et al. 2017)	Single moment with five categories of hydrometeor based on Pinty and Jabouille (1998) with modifications (Müller et al 2017)	RRTM (EcRad) With modified cloud optical properties compared to AROME-MF (Bengtsson et al. 2017)	Spectral/FD/NH

**Deleted:** Bastak-Duran

309 **3 Evaluation of basic surface meteorology and vertical profiles**

310 **3.1 Evaluation/Scores**

311 As mentioned in the introduction, the combination of MODFs and MMDFs allow detailed process-oriented diagnostics to be  
312 performed for the models. However, it is first important to assess what the errors are for standard variables such as 10m wind  
313 speed and 2m temperature. This first step is important because if they are stationary with leadtime one can simply consider a  
314 24hr time range in the forecasts such as T+25 until T+48 (the second day of the forecast), simplifying the analysis.

315

316 The 2m temperature errors [during February and March 2018](#) have quite different properties at each site and for each model  
317 (Fig 2). The models are typically too warm at Utqiāġvik and Tiksi and too cold at Ny-Ålesund and Whitehorse, with the sign  
318 of the bias varying between the models at Iqaluit and Eureka. At both Sodankylä and Whitehorse, which are situated at lower  
319 latitudes than the other sites, there is a distinct diurnal cycle in the bias and standard deviation that is not there at higher latitude  
320 sites. At both sites the night-time temperature bias is typically more positive than the daytime bias, indicating an underestimate  
321 of the diurnal temperature range. In the case of the CAPS and the IFS, the bias in the diurnal cycle at these observatories are  
322 representative of those seen over wider region (e.g. Casati et al., 2023 and Haiden et al., 2018).

323

324 In terms of wind speed, the forecasts all have a positive wind speed bias at Utqiāġvik and a negative bias at Iqaluit and  
325 Whitehorse (Fig 3). At Tiksi, Eureka, Sodankylä and Ny-Ålesund, the sign of the bias varies between the models. Interestingly,  
326 the largest inter-model spread and biases in wind speed is observed at the sites [surrounded by the most complex orography](#)  
327 (i.e. Iqaluit, Ny-Ålesund, Eureka and Tiksi: see Fig 2 of [Mariani et al., 2024](#)), likely due to the difficulties in representing the  
328 mesoscale flow patterns typically generated in such locations. Interestingly, there does not seem to be an obvious benefit from  
329 the increased resolution, with the AROME configurations and CAPS model actually having worse biases than the lower  
330 resolution global models at Ny-Ålesund.

331

332 Although there is some sub-daily variability with a diurnal frequency in the bias, more pronounced in wind speed bias (Figs.  
333 2 and 3), the size of the biases does not grow dramatically with time. Thus, we consider a 24hr time range between the T+25  
334 and T+48 forecast steps (i.e. the second day of the forecast) to be representative of the general error, simplifying the analysis.

335

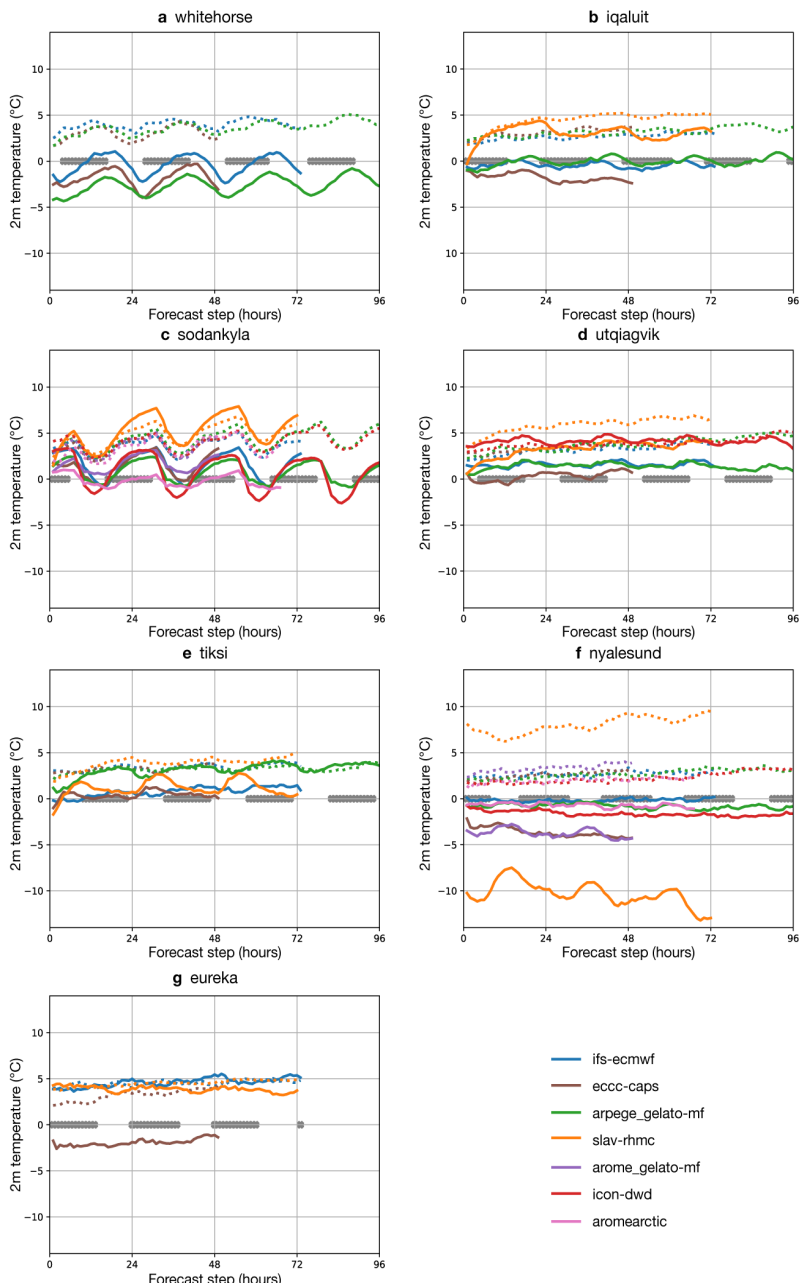
336

337

**Deleted:** with

**Deleted:** Morris

**Deleted:** 3

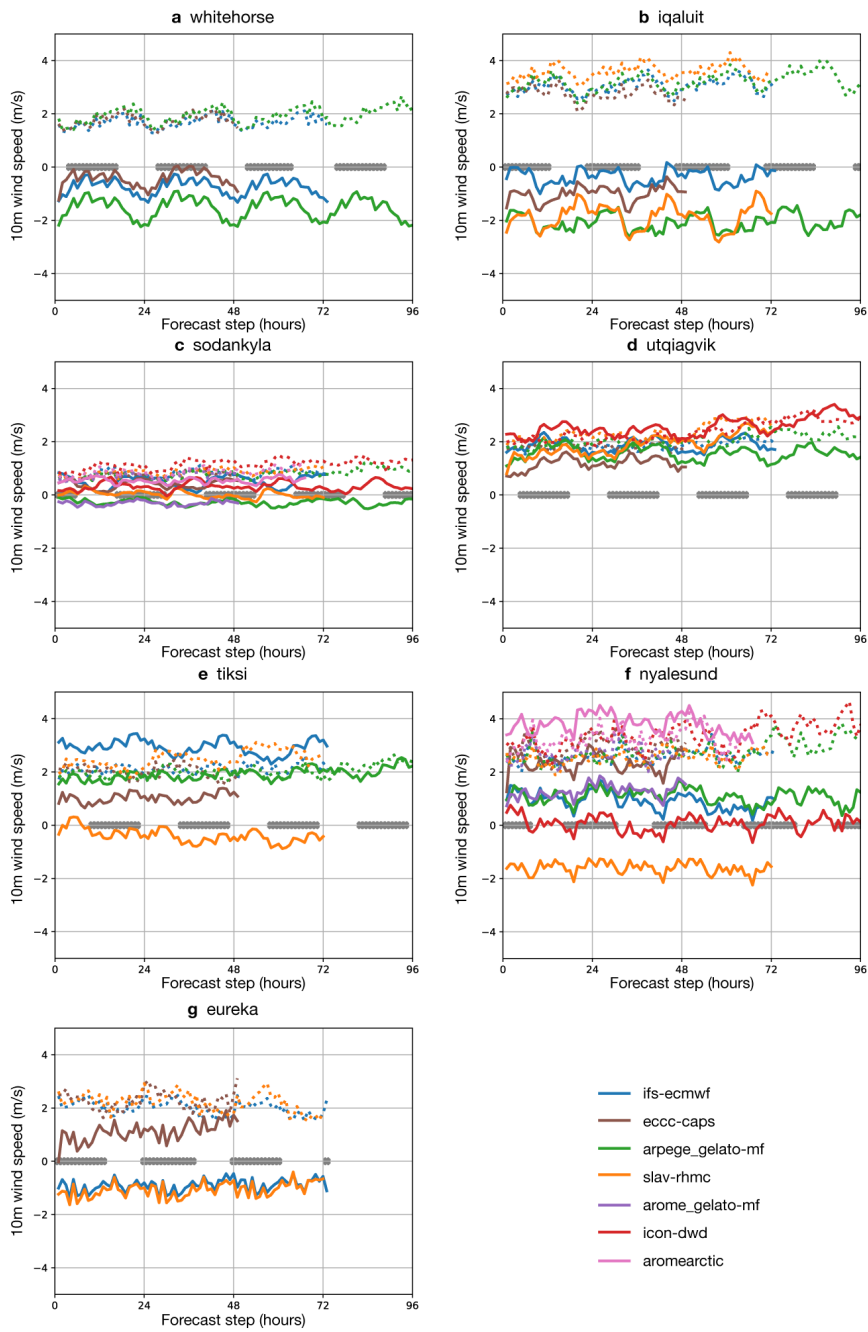


341  
342 **Figure 2: Mean bias (solid lines) and standard deviation (dashed lines) of the 2m temperature error (in °C) at each**  
343 **observatory (see Figure 1a) for forecasts initialised at 00z during SOP1, described in Table 2. Night-time periods (with**  
344 **mean  $SW \downarrow < 15 \text{ W m}^{-2}$ ) are indicated with grey crosses along the x-axis.**

341  
342 **Figure 2: Mean bias (solid lines) and standard deviation (dashed lines) of the 2m temperature error (in °C) at each**  
343 **observatory (see Figure 1a) for forecasts initialised at 00z during SOP1, described in Table 2. Night-time periods (with**  
344 **mean  $SW \downarrow < 15 \text{ W m}^{-2}$ ) are indicated with grey crosses along the x-axis.**

341  
342 **Figure 2: Mean bias (solid lines) and standard deviation (dashed lines) of the 2m temperature error (in °C) at each**  
343 **observatory (see Figure 1a) for forecasts initialised at 00z during SOP1, described in Table 2. Night-time periods (with**  
344 **mean  $SW \downarrow < 15 \text{ W m}^{-2}$ ) are indicated with grey crosses along the x-axis.**

341  
342 **Figure 2: Mean bias (solid lines) and standard deviation (dashed lines) of the 2m temperature error (in °C) at each**  
343 **observatory (see Figure 1a) for forecasts initialised at 00z during SOP1, described in Table 2. Night-time periods (with**  
344 **mean  $SW \downarrow < 15 \text{ W m}^{-2}$ ) are indicated with grey crosses along the x-axis.**



345  
346 **Figure 3: Mean bias (solid lines) and standard deviation (dashed lines) of the 10m wind speed error (in  $\text{m s}^{-1}$ ) at each**  
347 **observatory for forecasts initialised at 00z during SOP1. Night-time periods (with mean  $\text{SW} < 15 \text{Wm}^{-2}$ ) are indicated**  
348 **with grey crosses along the x-axis.**

349

350

351 **3.2 Vertical profiles**

352 To gain further insights we investigate the vertical structure of the errors by comparing the model output to observations from  
 353 radiosonde and tower. To do this the model and tower data were thinned to the same frequency as the radiosonde prior to  
 354 calculating the median and inter-quartile range shown in Figs 4 & 5. The median temperature and specific humidity within the  
 355 boundary layer is overestimated at Tiksi, Eureka, Utqiagvik and Iqaluit (see Fig 4) and the models underestimate the strength  
 356 of temperature and humidity inversions as a result. The picture is more mixed at Ny-Ålesund and Sodankylä where most  
 357 models are too cold and humid, and two out of the three models are too dry at Whitehorse.

358

359 The biases in the upper air temperatures, 2m air temperature, and the surface skin temperature tend to go hand-in-hand with  
 360 each other, i.e. model with warmest/coldest surface temperature tends to have the warmest/coldest 2m and upper air  
 361 temperatures. As a result, the mean 2m temperature errors seen in Fig 2 give a sense of the sign of the error in the lowest 100m,  
 362 or so, of the atmosphere. This coupling between the lowest model level, the surface skin temperature and the 2m-temperature  
 363 is to be expected, since the 2m-temperature is a diagnostic calculated as a function of the lowest atmospheric model layer and  
 364 the surface skin temperature.

365

366 Air temperature variability in the lower boundary layer is generally underestimated by the models, except at Iqaluit (Fig 5).  
 367 This generally translates to an underestimation of the 2m temperature variability at these sites. Interestingly, at Ny-Ålesund  
 368 some models severely overestimate the 2m temperature variability, despite underestimating the variability aloft, possibly due  
 369 to the overestimation of the surface skin temperature variability. For specific humidity the observed inter-quartile-range tends  
 370 to sit within the range of the models, however it is over-estimated at Eureka and underestimated at Tiksi and Whitehorse in  
 371 the lower boundary layer.

372

373 The median of the modelled wind speed is too high in the boundary layer at Sodankylä, Utqiagvik and Tiksi, but more mixed  
 374 at other sites (Fig 4 & 5). The variability of the wind speed is within the model range, with the exception of Iqaluit, where it  
 375 is underestimated. The overestimation of the wind speed at these sites is likely a contributing factor in the underestimation of  
 376 the temperature and humidity inversions, since a positive bias in the wind speed will drive excessive turbulent mixing of heat  
 377 and moisture inhibiting the decoupling of near-surface and upper air temperatures that occurs during periods of radiative  
 378 surface cooling and low wind (Van de Weil et al., 2017). Other factors which could play a role are the radiative forcing at the  
 379 surface or the response of the surface to radiative forcing. Both aspects will be addressed in the following subsection.

**Deleted:** Ny-Ålesund

**Deleted:** all

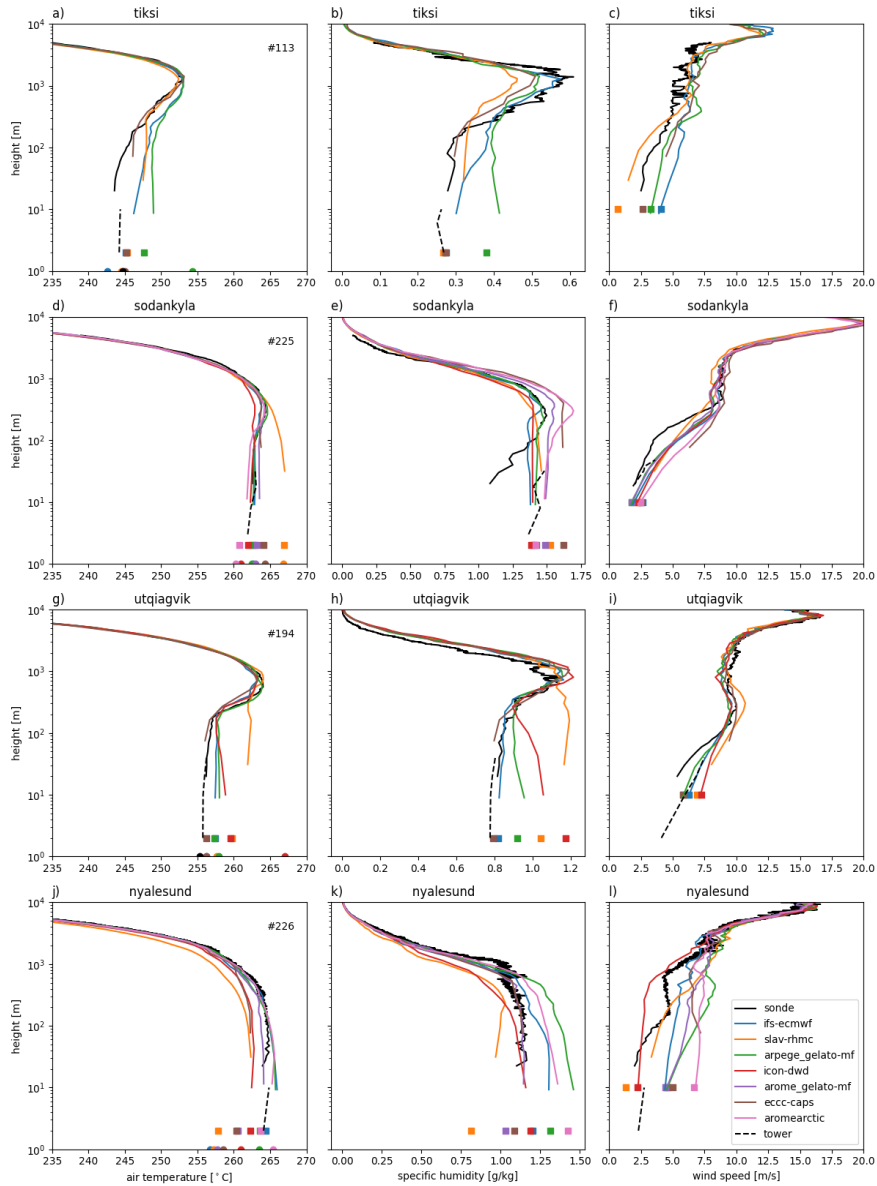
**Deleted:** Ny-Ålesund

**Deleted:** variance

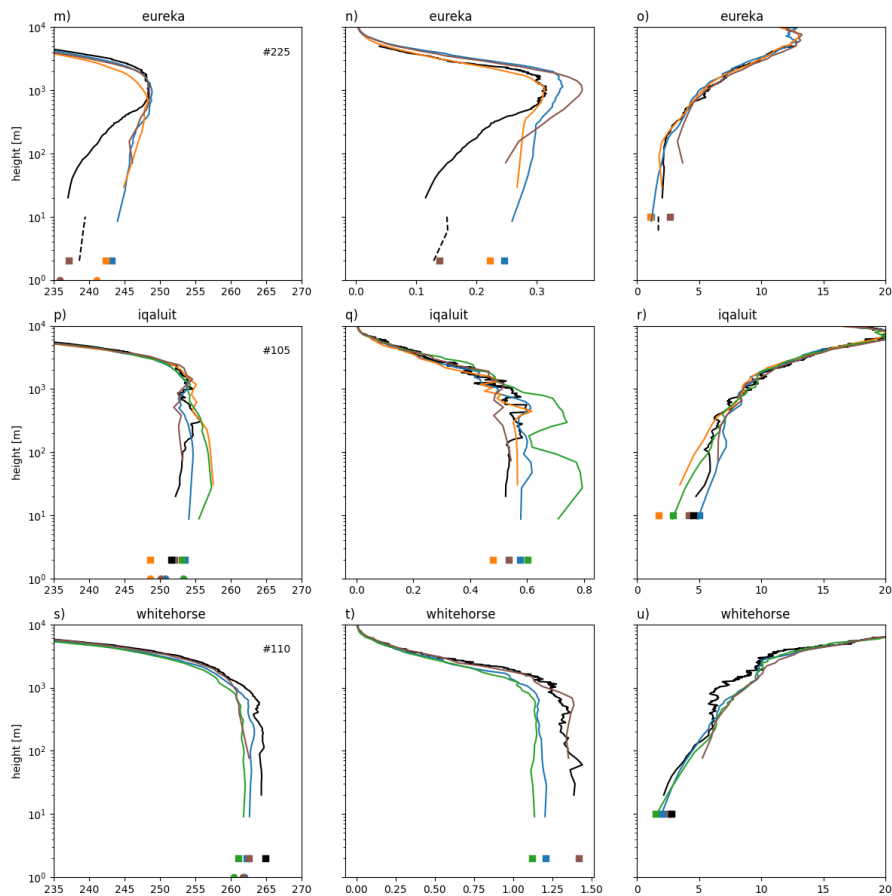
**Deleted:** variance

**Deleted:** variance

**Deleted:** Iqaluit



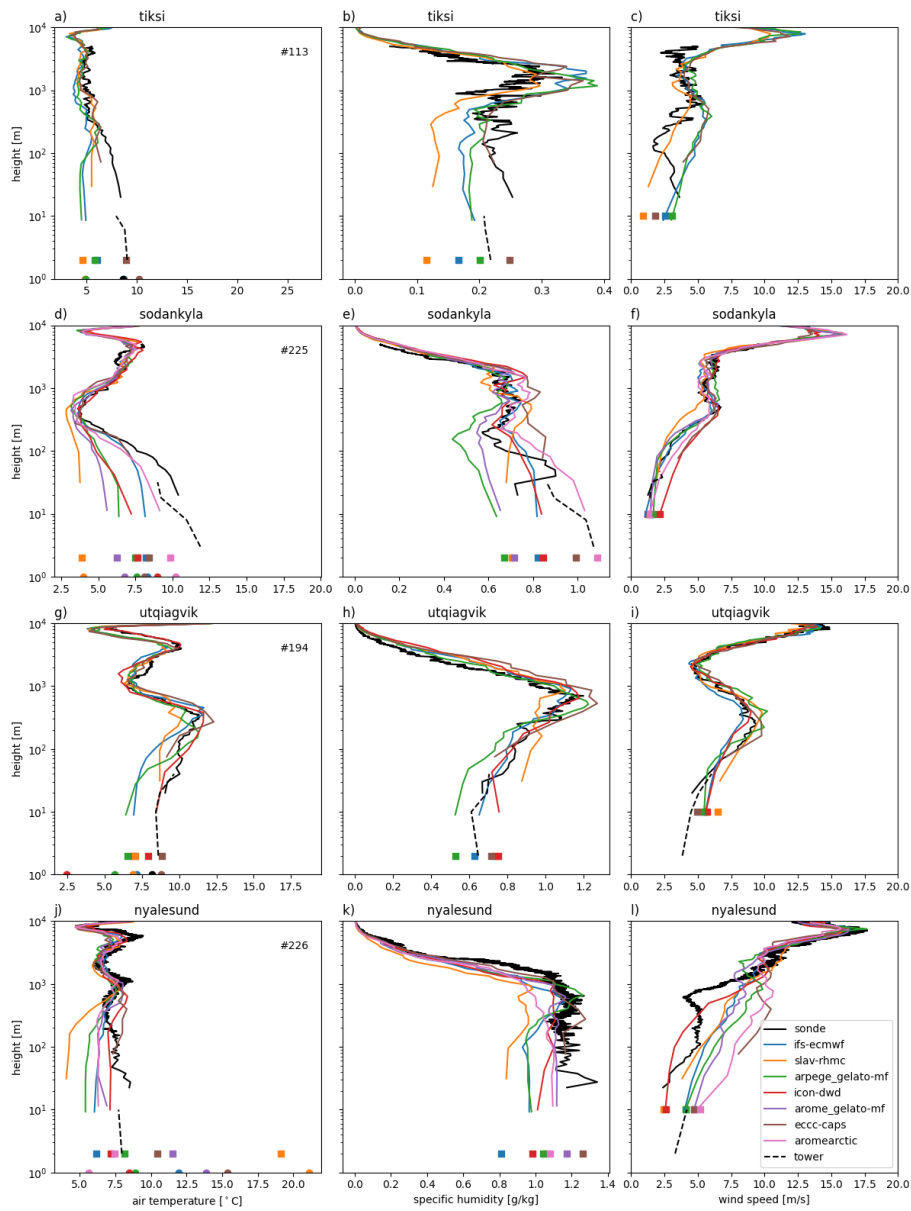
389 **Figure 4:** Median temperature (left), specific humidity (middle) and wind speed (right) from the radiosonde (black  
 390 solid line), the tower (black dashed line), and the numerical models (during the second day of the forecast: colour lines).  
 391 The mean surface skin temperature is indicated by a dot, 2m temperature (left), 2m specific humidity (middle) and  
 392 10m wind speed (right) are shown with a square. Note that wind speed and humidity profiles from the tower are not  
 393 available in the Tiksi and Ny-Ålesund MODFs respectively. The numbers in the left hand panels correspond to the  
 394 verification sample size, which was dictated by the availability of radiosonde profiles.



395

396 **Fig 4 continued.**

397

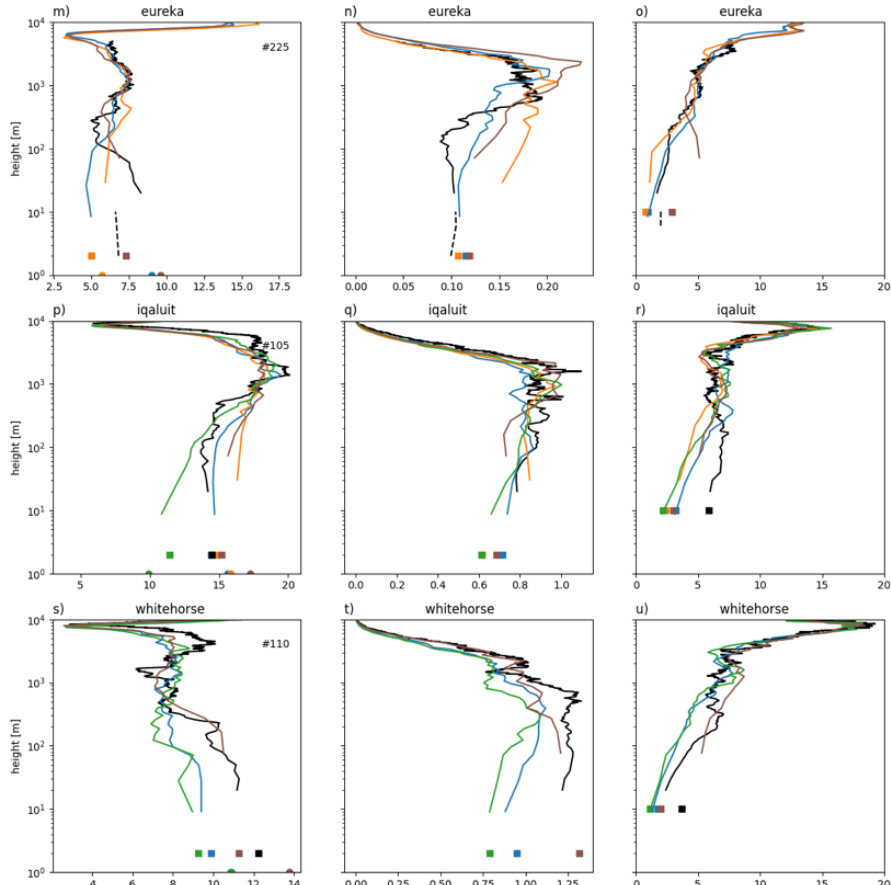


398

399

400 **Figure 5: As Figure 4 but showing the Inter Quartile Range.**

401



402  
403 **Fig 5 continued.**

404  
405 **3.3 Links between errors in boundary-layer temperature variability and surface radiation.**

406 In this section we investigate the role of radiative forcing in the underestimation of near-surface and boundary-layer  
407 temperature variability at Sodankylä, Utqiagvik and Tiksi where the models underestimate the temperature variability. At these  
408 sites all upwelling and downwelling radiation components are available in the SOP1 MODFs allowing us to investigate  
409 whether the suppressed temperature variability is related to suppressed variability in the radiative forcing at the surface, a lack  
410 of sensitivity of the near-surface temperature to radiative forcing or something else.

**Deleted:** nce

411  
412 The box-plots shown in Fig 6a-c confirm the underestimate of near-surface-temperature Inter-Quartile Range (IQR) at Tiksi  
413 (except CAPS), Sodankylä, and Utqiagvik, and further show that the cold tail of the distribution is generally shorter in the  
414 models meaning there is a warm bias during cold periods. The warm bias in cold conditions is well known at Sodankylä and  
415 is typical of NWP systems (see Atlaskin and Vihma, 2012 and Day et al., 2020), but this feature has not been shown before at  
416 the other two sites to our knowledge.

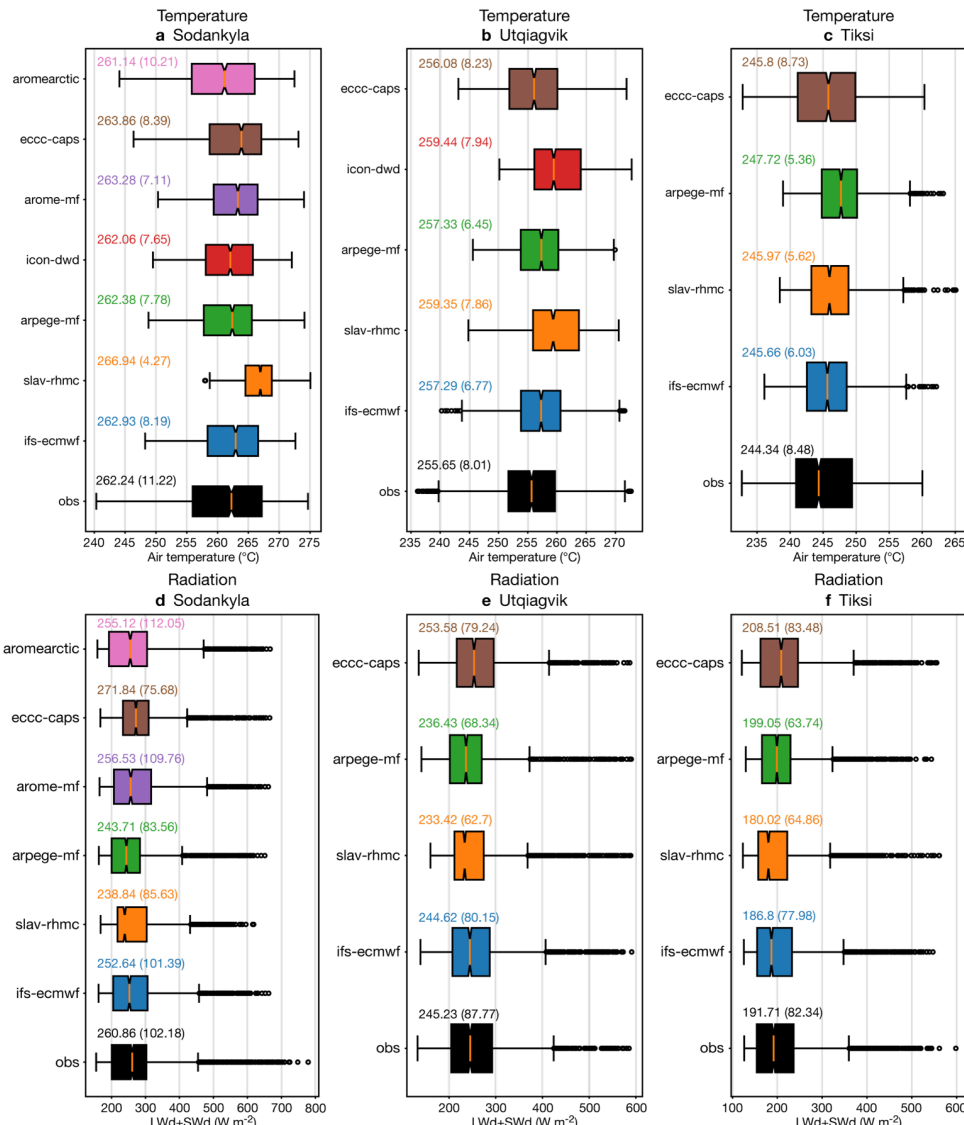
**Deleted:** supressed

**Deleted:**

421 The models typically also show differences in the distribution of the downwelling radiation at the surface,  $LW \downarrow + SW \downarrow$   
422 compared to observations (Fig 6d-f). The IQR is underestimated at Tiksi (except for CAPS) and Utqiagvik. However, at  
423 Sodankylä all the models overestimate the IQR (except for CAPS) but also do not capture the highest values of incident  
424 radiation observed at the top of the distribution. Since errors in the incident radiation likely relate to interactions with clouds,  
425 which are not included in this iteration of the MODFs, we will not investigate the causes of these discrepancies between the  
426 observed and forecast radiation distributions further, leaving this for a more focussed future study, and will instead move on  
427 to focus on the response of the near-surface air temperature and the surface energy budget.

428  
429  
430  
431  
432  
433  
434  
435  
436  
437  
438  
439  
440  
441  
442  
443  
444

**Deleted:** In this study we



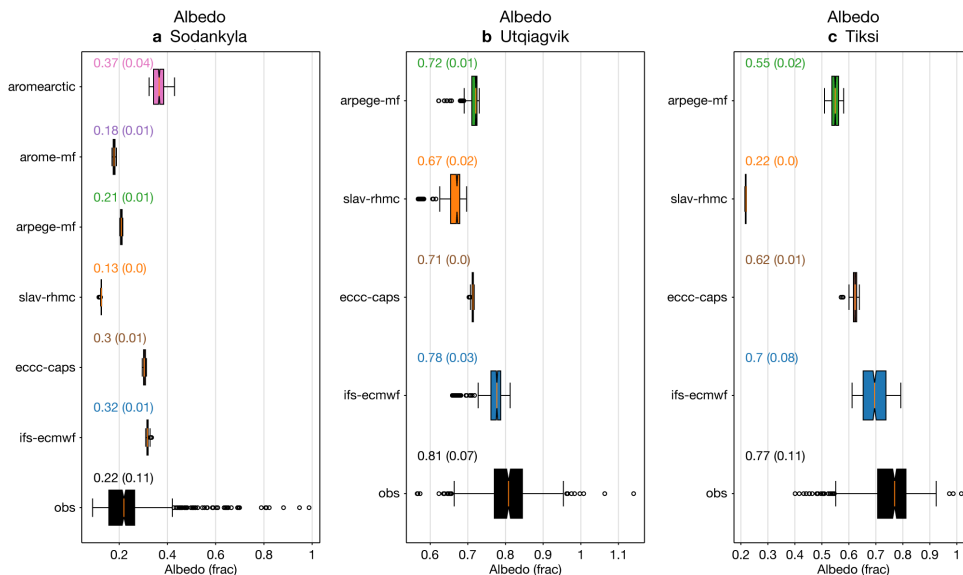
448 **Fig 6. Boxplots of T2m (a-c) and LW↓+SW↓ (d-f) for Sodankylä, Utqiagvik and Tiksi in observations and during the  
449 second day of the forecast. The text above the boxplots states the median (and inter-quartile-range) of each distribution,  
450 which are also shown by the orange line and box edges respectively. The 5-95% range is plotted by the whiskers and  
451 points outside this are shown in dots.**

453 As  $LW\downarrow + SW_{net}$  is the effective radiative forcing for the surface skin temperature (and indirectly for the 2m temperature),  
454 errors in 2 m air temperature are either due to errors in this driving term itself, the relationship between  $LW\downarrow + SW_{net}$  and 2 m

**Deleted:** to

**Deleted:** a major driver of 2 m air temperature

457 temperature, or a more likely combination of both (assuming that errors in advection are negligible). Because the model median  
 458 surface albedo (except for SLAV at Tiksi) is close to the observed estimate (Fig 7), then we can focus on how 2m temperature  
 459 varies as a function of  $LW/ + SW_{net}$  to more deeply investigate the causes of error.



462  
 463 **Figure 7. Boxplots of surface albedo for Sodankylä, Utqiagvik and Tiksi in observations and during the second day of**  
 464 **the forecast. The text above the boxplots states the median (and inter-quartile-range) of each distribution, which are**  
 465 **also shown by the orange line and box edges respectively. The 5-95% range is plotted by the whiskers and points outside**  
 466 **this are shown in dots.**

467  
 468 At Sodankylä, Tiksi and Utqiagvik all the models have a warm 2m temperature bias at low levels of incoming radiation ( $LW/ + SW_{net}$ ) (see Fig 8). At Tiksi, Utqiagvik and Sodankylä the overall sensitivity of T2m to radiative forcing, as measured by the  
 469 slope of the regression coefficient between 2m-temperature and  $LW/ + SW_{net}$  is underestimated in all the models with one  
 470 exception. [The AROME-Arctic model seems to be too sensitive at Sodankylä according to this diagnostic, but captures the  
 471 observed temperature range at low levels of  $LW/ + SW_{net}$ .]

472  
 473 Note that the LW components used for Sodankylä in this study, are not those provided in the SOP1 MODF, which are collected  
 474 at the top of the 45m tower, rather they are from a dedicated radiation tower located near the sounding station where the  
 475 downwelling component is at a height of 16m and the outgoing is at 2m. These were swapped due to a concern over the  
 476 accuracy of the LW radiation data collected at the met tower (Roberta Pirazzini, personal communication).

**Deleted:** we find that, with the exception of the SLAV model at Tiksi, ...

**Deleted:** investigate

**Deleted:** So looking at how the

**Deleted:** can

**Deleted:** provide additional information on

**Commented [1]:** why the observed albedo sometimes exceeds 1? why the spread of the obs albedo is so much larger than the one for the models?

**Commented [2R1]:** I think this is because when the sun is close to the horizon, as is at this time of the year, the "upward" sensor at 2m will sometimes be getting direct sunlight. I wonder if it is worth mentioning this. In the models it's just a lookup table for the surface type. I don't have a good explanation for the spread. Other than observations being noisy. I suspect it may not reflect true variability in the actual surface albedo. Although I suspect the true answer is somewhere in the middle.

**Deleted:** 1

**Deleted:** conditional

**Deleted:** 7

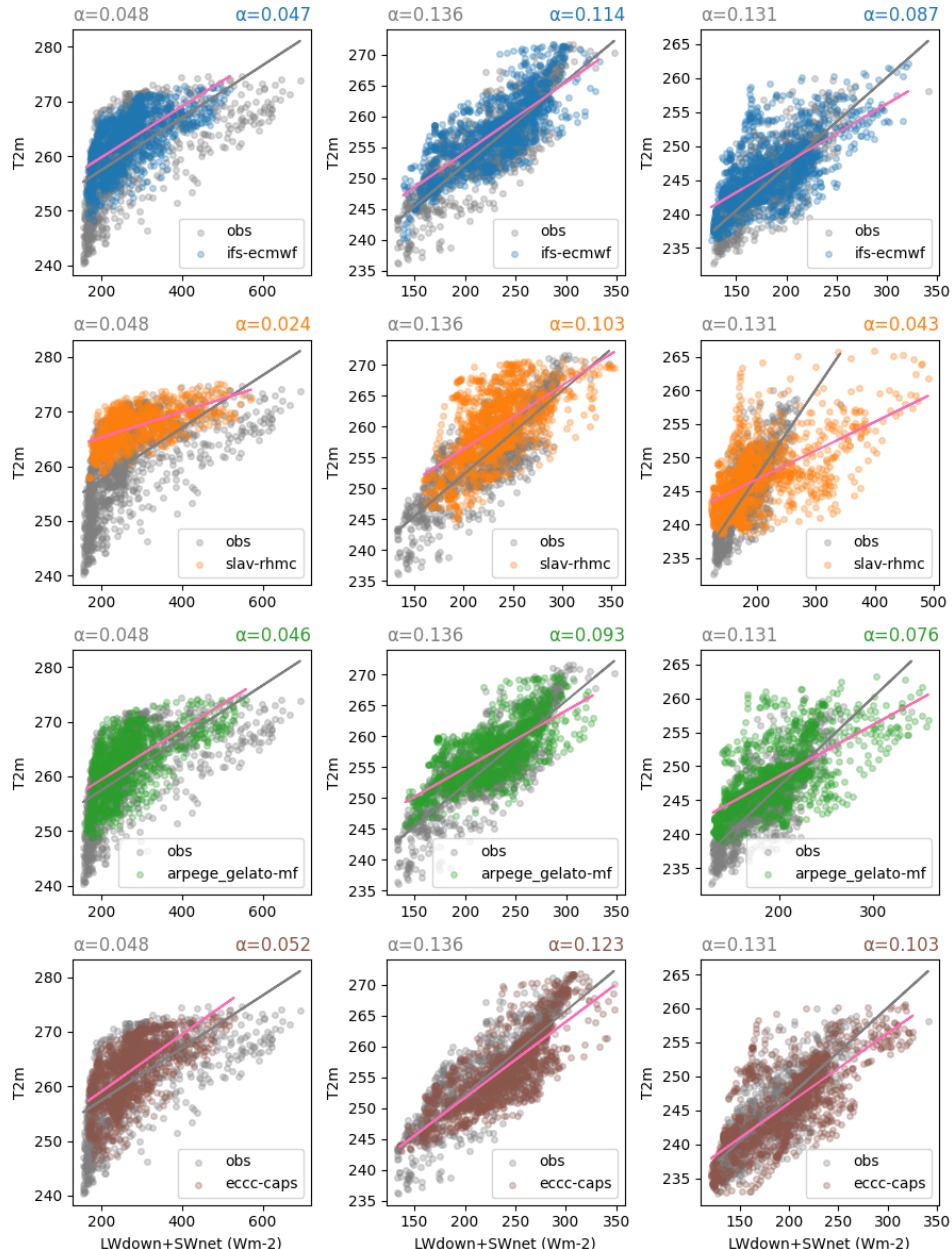
**Deleted:** is actually

**Deleted:** ,

**Commented [3]:** The relationship between T2m and  $LW_{down} + SW_{net}$  is not linear in Sodankylä, not for observations and not for models. There is snow on the ground which limits the temperatures to rise much above 0 degC no matter how much radiative forcing there is. When fitting a linear line into the data, it indeed looks like AROME-Arctic is too sensitive. But this is mainly because lack of high values of  $LW_{down} + SW_{net}$ , and not because the model is too sensitive in the cold end.

**Commented [4R3]:** It would actually be interesting to have a look at these sensitivities conditionally by stability ( $Ri$ ) or simply binned by intervals of  $LW_{down} + SW_{net}$ . I am not asking you to revise the paper at this stage, especially because reviewers didn't comment this part, but concluding that AROME-Arctic is too sensitive is a bit contrary what we see.

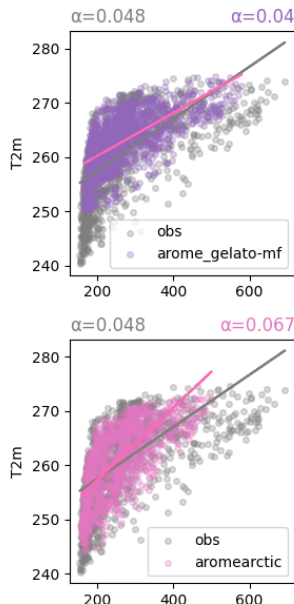
**Commented [5R3]:** Agree this would be interesting to look at.



489  
490 **Figure 8:** Scatter plots of 2m temperature as a function of  $LW_{down} + SW_{net}$  for Sodankylä, Utqiagvik and Tiksi (from left  
491 to right), for the second day of the forecast. The regression slope between the 2m temperature and the  $LW_{down} + SW_{net}$  is  
492 stated in the title, for the observations (in grey) and each model (various colours).

Deleted: 7

Deleted: during the second day of the forecast

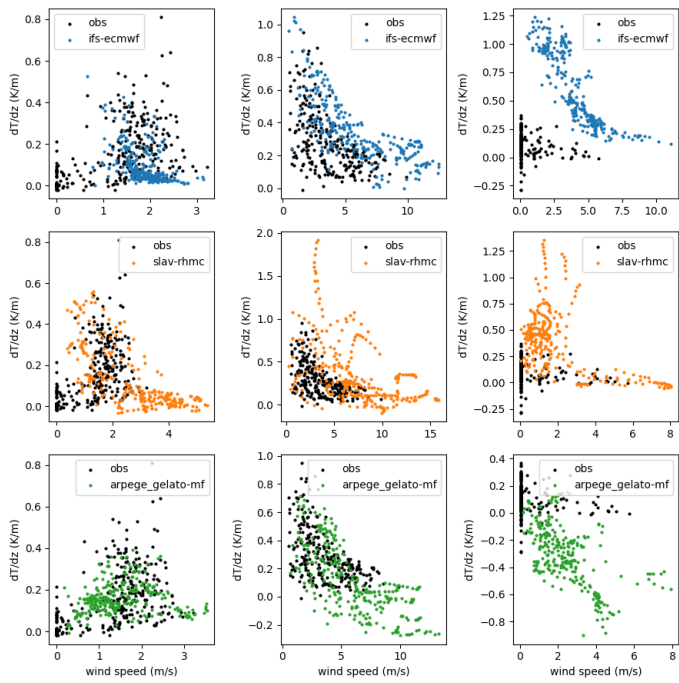


497 **Figure 8. cont.**

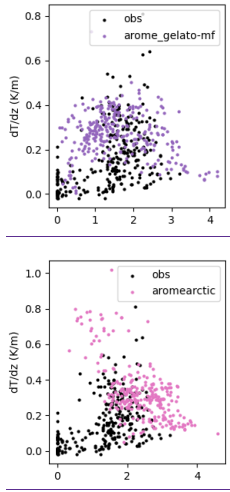
Deleted: 7

498  
499 To investigate the role of surface-atmosphere decoupling in the 2m-temperature cold-tail warm bias and lack of 2m-  
500 temperature variability at low levels of incident radiation we plot the thermal stratification as a function of near-surface wind  
501 speed at the three sites (Fig 9) for situations where the model or observed  $LW\downarrow + SW_{net}$  is below the 20<sup>th</sup> percentile. In the  
502 observations one can see the typical pattern seen at other sites (e.g. Ven de Weil et al., 2016) that inversions are weak for  
503 strong winds, whereas large inversions are found under weak-wind conditions with a transition found between those regimes  
504 at some critical wind speed. The models generally capture this qualitative regime behaviour (Fig 9), although the magnitude  
505 of the thermal stratification, the wind speed and the critical wind speed for the regime transition varies between the models.

Formatted: Superscript



508  
509 **Figure 9. Scatter plots of thermal stratification ( $(T_{2m}-T_{lm})/\text{height}$ ) as a function of wind speed on the lowest model at**  
510 **Sodankylä, Utqiagvik and Tiksi (from left to right) for the observations (in black)**  
511 **and each model (various colours)**  
512 **during the second day of the forecast for situations where the model or observed  $LW_{\downarrow} + SW_{\text{ret}}$  is below the 20th**  
513 **percentile.**



514  
515 **Figure 9. continued.**

516  
517 Formatted: Subscript  
518 Deleted: grey  
519 Formatted: Font: Italic  
520 Formatted: Font: Italic, Subscript

518  
519

520 **3.4 Surface energy budget sensitivity to radiative forcing**

521 Further insight into the role of the land-surface and surface exchange processes in the T2m errors outlined in the previous  
522 section, particularly the lack of T2m sensitivity to radiative forcing, can be gained by constructing surface energy budget  
523 sensitivity diagrams, following Miller et al. (2018) and Day et al. (2020). The idea here is that the surface energy budget can  
524 be separated into a “driving term” ( $LW\downarrow + SW_{net}$ ) and “response terms” (SHF, LHF, GHF, and  $LW\uparrow$ ). The relationship  
525 between the driving term and each response term can be summarised with regression coefficients, e.g. for the SHF:

526 
$$SHF = \alpha_{SHF}(LW\downarrow + SW_{net}) + \beta_{SHF} \# (1)$$

527 where each of the  $\alpha$ 's can be interpreted as a coupling strength parameter between the driving term and each response term.  
528 These  $\alpha$ 's provide direct information on the proportional response of each flux term, expressed as a fraction of the total change  
529 in radiative forcing. From this one can see that if, for example, the coupling to the ground heat flux and turbulent fluxes is too  
530 strong in the model (i.e.  $|\alpha_{GHF_{mod}} + \alpha_{SHF_{mod}} + \alpha_{LHF_{mod}}| > |\alpha_{GHF_{obs}} + \alpha_{SHF_{obs}} + \alpha_{LHF_{obs}}|$ ) then  $|\alpha_{LW\uparrow}|$  will be too small, i.e.  
531 surface temperature response will be too weak and vice versa. Similarly, compensating errors in the strength of the coupling  
532 to the turbulent fluxes ( $\alpha_{SHF_{mod}} + \alpha_{LHF_{mod}}$ ) and ground heat flux ( $\alpha_{GHF_{mod}}$ ) could result in the right surface-temperature  
533 sensitivity,  $\alpha_{LW\uparrow}$ , but for the wrong reasons. As a result, by comparing the observed and modelled regression coefficients one  
534 can derive physical understanding of the causes of model error.

535

536 Note that in convective cases - the main driver of turbulent heat fluxes is indeed the convective instability at the surface driven  
537 by radiative forcing. However, in stratified conditions the main driver of turbulence in the boundary layer (and of the sensible  
538 and latent heat fluxes) is the mechanical forcing i.e. the large-scale wind speed (Van Hooijdonk et al. 2015, Van de Wiel et al.  
539 2017, Vignon et al. 2017). As a result, one expects the turbulent fluxes to have little sensitivity to the radiative forcing in stable  
540 conditions, with the ground heat flux taking a larger role in balancing changes in radiative forcing and the converse in  
541 convective cases (see Day et al., 2020). As a result, at Utqiāġvik and Tiksi where stable conditions dominate, the ground heat  
542 flux varies with changes in radiative forcing, more than the turbulent fluxes as indicated by higher regression coefficients. At  
543 Sodankylä there is more of an even partitioning between the turbulent fluxes and the ground heat flux into the snow.

544

545 It is clear from Figures 10, 11, and 12 that all the models generally underestimate the surface temperature sensitivity to radiative  
546 forcing at Sodankylä, Utqiāġvik and Tiksi, because the rate of change in  $LW\uparrow$  with changes in radiative forcing,  $LW\downarrow + SW_{net}$ ,  
547 i.e.  $\alpha_{LW\uparrow}$  is typically too low (i.e.  $\alpha_{LW\uparrow_{mod}} < \alpha_{LW\uparrow_{obs}}$ ). Since the 2m temperature diagnostic in the models is calculated as a  
548 function of the surface skin temperature, the underestimation of the 2m-temperature and  $LW\uparrow$  sensitivity to radiative forcing  
549 and the positive bias in those variables in cold conditions are likely to be closely related (i.e. comparing Fig 8 to Figs 10, 11  
550 and 12). For example, at Sodankylä the CAPS model T2m and upwelling longwave ( $LW\uparrow$ ) sensitivities are very close to what  
551 is observed, AROME-Arctic slightly overestimates these sensitivities and SLAV underestimates them. A similar  
552 proportionality can be seen between these properties of the models at the other two sites. Note that because the  $LW\uparrow$  at  
553 Sodankylä was observed at 2m and so has rather a small footprint compared to the sensor on the 16m mast, the sensitivity is  
554 more representative of the bare snow than the forest canopy. As a result, one might expect the area mean  $LW\uparrow$  sensitivity to  
555 be higher than the value presented here.

556

557 This mismatch in terms of  $LW\uparrow$  sensitivity goes hand in hand with differences in the other  $\alpha$  coefficients and by comparing  
558 the sensitivities of the other response terms in the surface energy budget we can develop some hypotheses about what is leading  
559 to this mismatch in surface temperature sensitivities. For example, at Utqiāġvik, all the models tend to overestimate the

**Deleted:** 8

**Deleted:** 9

**Deleted:** 0

**Deleted:** sensitivity parameter (the regression coefficient) for

**Deleted:** inability of the models to capture the lowest values of these ...

**Deleted:** 7

**Deleted:** 8

**Deleted:** 9

**Deleted:** 0

**Deleted:** it

571 sensitivity of the  $GHF$ ,  $\alpha_{GHF}$ , which was calculated as the residual of the observed radiative and turbulent fluxes. This can be  
572 an indication of an indication of non-sufficient thermal representation of the land surface, for example lack of a multi-layer  
573 snow model (e.g. Day et al., 2020; Arduini et al., 2019). Unfortunately, we are not able to perform a similar calculation as  
574 performed for Sodankylä, to estimate the  $GHF$ , as the longwave observations thought to be most reliable, are not co-located  
575 with the other flux observations, or Tiksi, since we don't have the turbulent fluxes in the MODF. As a result, we cannot  
576 calculate the  $GHF$  as a residual of the other terms.

577

578 Where we have turbulent flux observations, we can also evaluate the  $\alpha_{SHF}$  and  $\alpha_{LHF}$  terms. At Utqiāġvik, an underestimation  
579 of the sensitivity of the turbulent fluxes, too low  $\alpha_{SHF}$  and  $\alpha_{LHF}$  in the ARPEGE and SLAV models goes hand in hand with an  
580 overestimation of  $\alpha_{GHF}$  mentioned above. In the IFS and ECCC models are closer to observations with smaller values of  $\alpha_{GHF}$   
581 and larger values of  $\alpha_{SHF}$  and  $\alpha_{LHF}$ . At Sodankylä, the  $\alpha_{SHF}$  varies quite a bit from model to model, but all the models where  
582 the LHF was available overestimate the  $\alpha_{LHF}$ .

583

584 At all three sites the relative size of the coefficients varies between the sites, with  $\alpha_{LW1}$ ,  $\alpha_{SHF}$ ,  $\alpha_{GHF}$  typically being an order  
585 of magnitude larger than  $\alpha_{LHF}$ . This is likely to be typical of cold dry snow-covered environments where the magnitude of the  
586 latent heat flux is low. However, the difference in the relative size of the other three terms varies quite a bit between sites with,  
587 for example, the turbulent flux playing a larger role at Sodankylä than at Tiksi and Utqiāġvik at this time of year. This reflects  
588 the larger surface roughness at Sodankylä associated with the trees at this site.

589

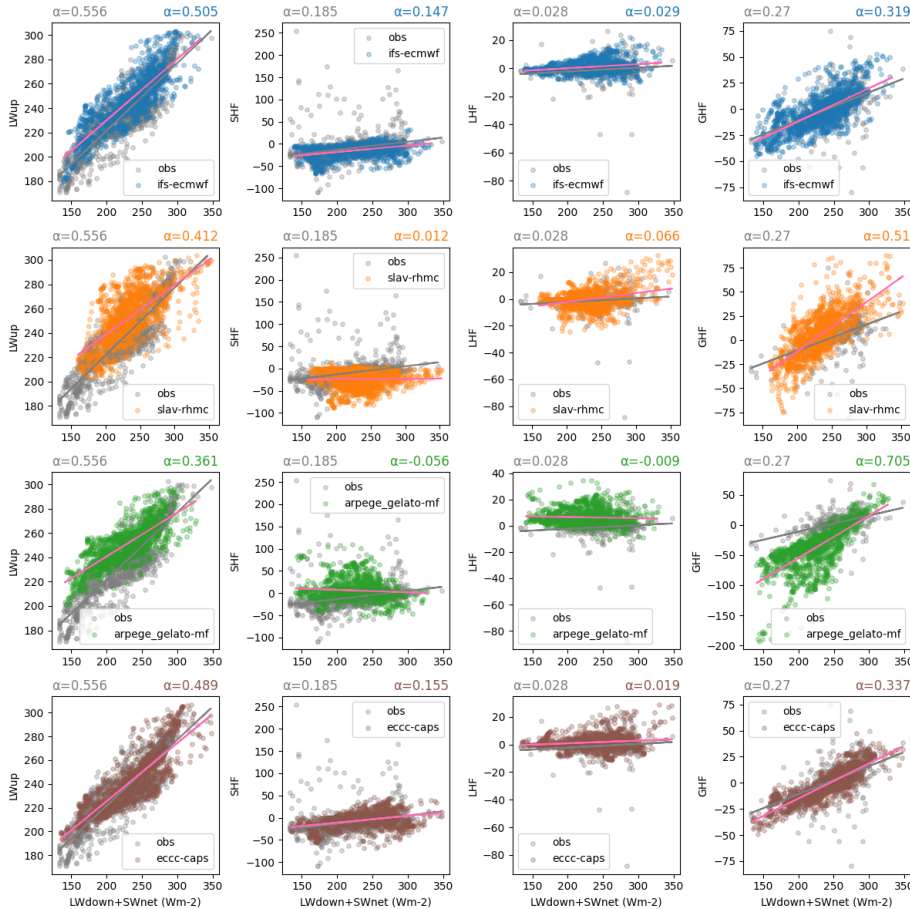
590 Before moving on it is worth noting that as well as being used to develop hypotheses about the causes of errors related to the  
591 surface energy budget, these process diagrams and sensitivity metrics could also be applied to test new configurations of NWP  
592 systems with modifications to the land-surface, boundary layer or related schemes and evaluate whether such modifications  
593 are improving the dynamic behaviour with respect to the surface energy budget in line with observed behaviour or not.

594

595

596

597



598

599 **Figure 10:** Process relationship diagrams and sensitivity parameters for upwelling longwave radiation (LWUp; left),  
600 sensible heat flux (SHF; middle left), latent heat flux (LHF; middle right) and ground heat flux (GHF; right) at  
601 Utqiāġvik. Observed values are shown in grey, model values during the second day of the forecast are shown in colour.  
602 The line of best linear fit is shown for observations (gray line) and each model (pink line). The sensitivity parameters,  
603  $\alpha$ , describing the coupling strength between the driving ( $LW\downarrow + SW_{net}$ ) and each response term are printed above each  
604 diagram, with observational (modelled) relationship on the left (right).

605

606

Deleted: 8

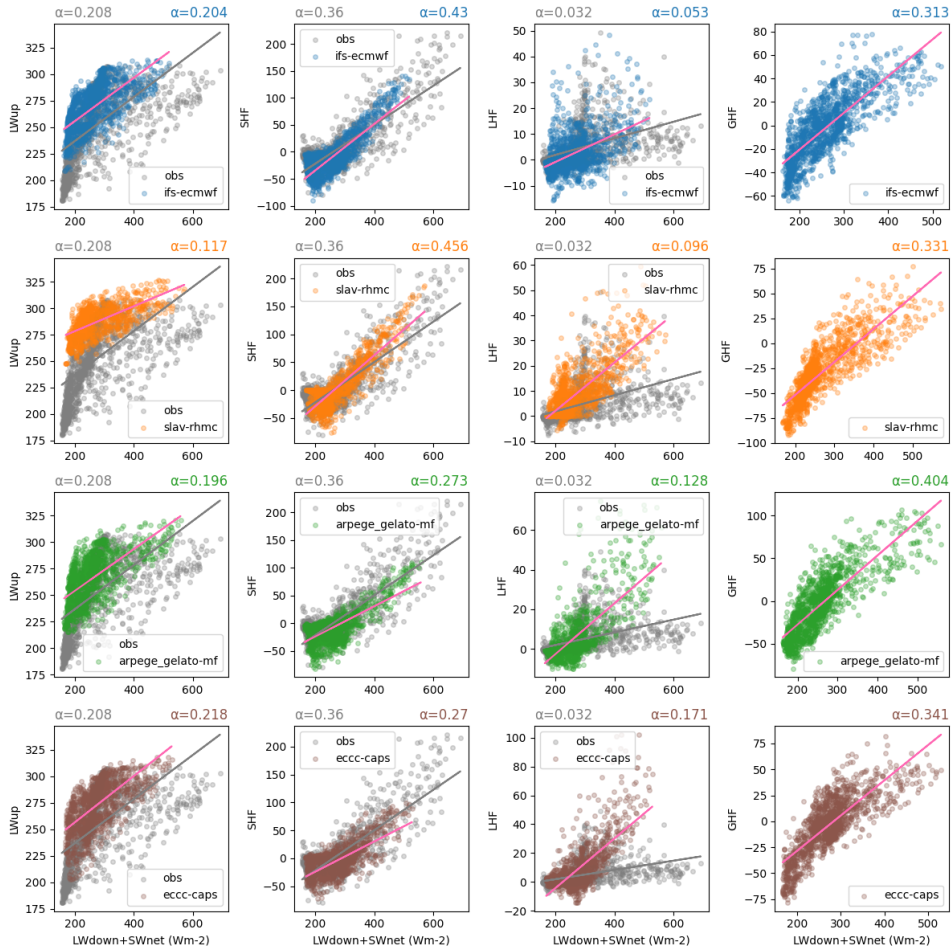


Figure 11: Same as Figure 8 but for Sodankylä.

Deleted: 9

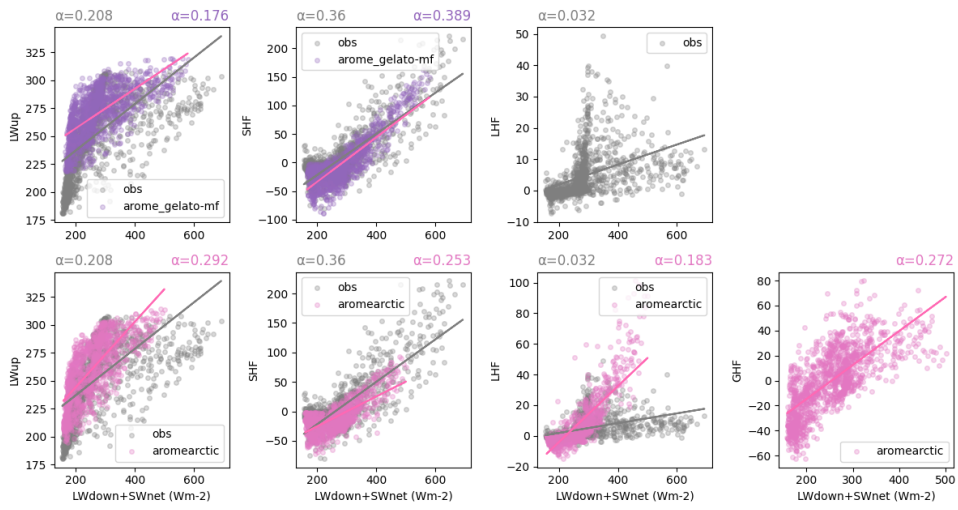
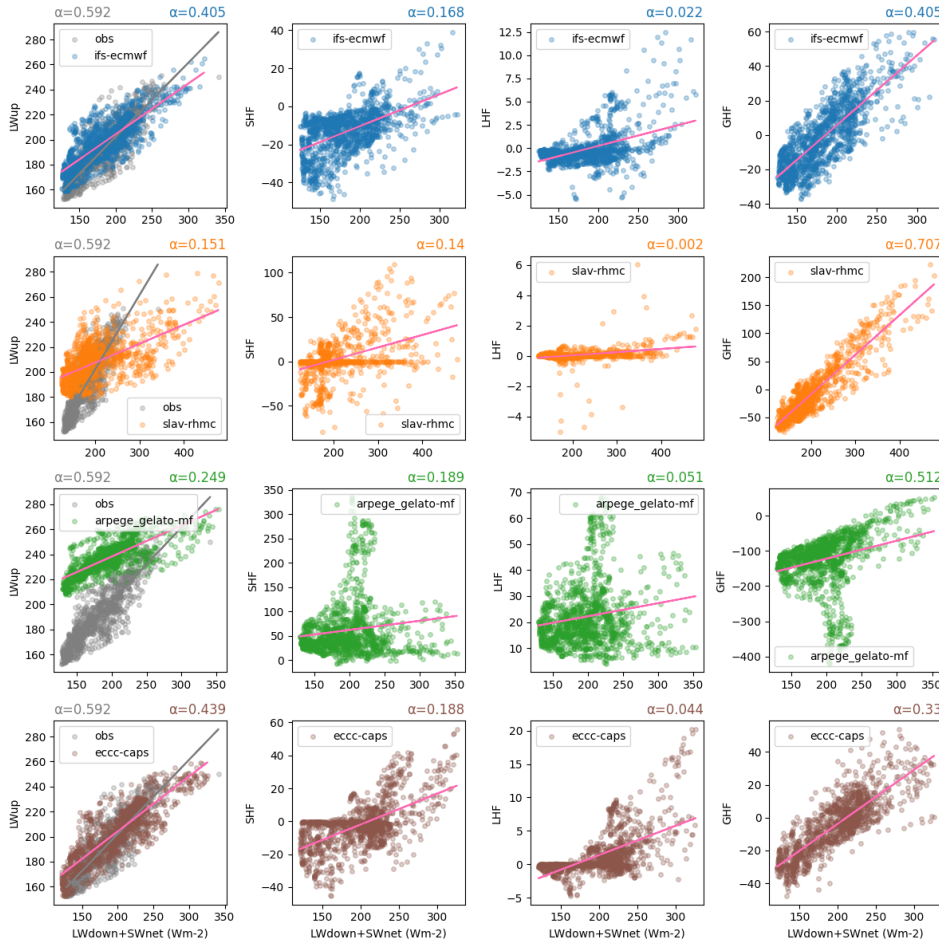


Figure 11: cont.

Deleted: 9



620  
621 **Figure 12:** Same as Figure 8 but for Tiksi.  
622

**Deleted: 0**

623 **3.5 Evaluation of wind stress and sensible heat flux**

624 The previous examples highlight discrepancies between forecast and observations and provide hints as to which processes are  
625 responsible for the documented errors. The observed conditions also provide multi-variate targets for updated forecasting  
626 systems. However, the observations can also help us evaluate a specific process and thereby target a specific parameter or  
627 parameterization to change.

628  
629 The Sodankylä and Utqiāġvik MODFs include turbulent fluxes and profiles of wind speed and temperature allowing us to  
630 investigate the parameterisation of turbulent exchanges of heat and momentum at the surface. Turbulent surface fluxes in NWP  
631 models are often parameterised according to Monin-Obukhov (M-O) similarity theory where they are related to the gradient  
632 in the lowest atmosphere (e.g. Beljaars and Holtslag, 1991):

$$\tau = \rho C_M U_{ref}^2 \#(2)$$

$$SHF = \rho C_H U_{ref} (\theta_{ref} - \theta_{fc}) \#(3)$$

**Deleted: p**

637 where  $\tau$  is the wind stress,  $U$  is the wind speed,  $\theta$  is potential temperature,  $\rho$  is the air density and the transfer coefficients,  $C_M$   
638 and  $C_H$ , used to in each computation, are a function of the roughness length of momentum and heat,  $z_{0M}$  and  $z_{0H}$ , and a stability  
639 parameter. In these equations the  $U_{ref}$  and  $\theta_{ref}$  are the wind speed and potential temperature at a reference height, which in the  
640 case of the models is the lowest atmospheric model level, the height of which varies from around 10 to 30 m above the surface  
641 depending on the model (see Table 3).

642  
643 Successfully parameterizing  $\tau$  and  $SHF$  relies on defining a reasonable function for  $C_M$  and  $C_H$  and selecting the appropriate  
644 parameters and a proper aggregation of the fluxes in the cases of a tiled surface. Because we have observed and forecast values  
645 for both the fluxes and the bulk parameters in equations 2 and 3 we can diagnose how appropriate the choices in each model  
646 are for the conditions at a particular site. This is done by examining the relationship between the bulk parameters,  $U$  and  $\theta$ ,  
647 and the fluxes  $\tau$  and  $SHF$  (see Figures 13 to 16, as done previously by Tjernström et al. (2005) and more recently by Day et  
648 al. (2020)).

649  
650 In the case of wind stress, in neutral conditions, the points in Figures 13 and 14 would sit on the straight line following:

$$\tau = \rho \frac{k^2 U^2}{\left[ \ln \left( \frac{z_{ref}}{z_{0M}} \right) \right]} \quad \#(4)$$

651 where  $z_{ref}$  is the height of the lowest model level,  $k$  is the von Karman constant and  $z_{0m}$  is the aerodynamic roughness length.  
652 The slope of this line is determined by  $z_{0m}$ . However, this formula provides an overly simplified view as the atmospheric  
653 stability varies from neutral conditions and as a result there is scatter in the values of  $\tau$  for any given wind speed.

654  
655 The relationship between  $\tau$  and  $U$  for Sodankylä (Figure 13) differs between the models and between the models and the  
656 observations. An estimate of the observed roughness length was calculated, following the equation above, after selecting for  
657 neutral conditions, and the value is presented in Table 4 along with the value used in each of the models. In the AROME-  
658 Arctic and ICON models,  $\tau$  increases too slowly with increasing  $U$ . This is consistent with the fact that the roughness length  
659 for momentum is too low in these models, which have roughness lengths an order of magnitude lower than that derived from  
660 observations (see Table 4). Increasing  $z_{0m}$  in the AROME-Arctic and ICON models would likely reduce the positive bias in  
661 the wind median wind speed profile seen in Figure 4, however the other models which have roughness lengths closer to what  
662 was observed also have a positive wind speed bias suggesting another cause.

663  
664 Interestingly, all models fail to adequately capture the spread of  $\tau$  for a given value of  $U$ , likely because the models  
665 underestimate the atmospheric stability as is suggested by the weaker than observed thermal stratification indicated by in Figs  
666 4d and 5d. A more detailed study including numerical experimentation would be needed to demonstrate this further.

667  
668 At Utqiagvik, the aerodynamic roughness length is three orders of magnitude lower than at Sodankylä, reflecting the difference  
669 in surface type: snow covered tundra compared to the forested taiga of northern Finland (Table 4). Here the IFS and SLAV  
670 models have roughness lengths close to those derived from observations, whereas the ARPEGE and ICON have values that  
671 are higher. As a result, for a given wind speed the surface stress is too high in these two models (Figure 14).

Deleted: 1

Deleted: 4

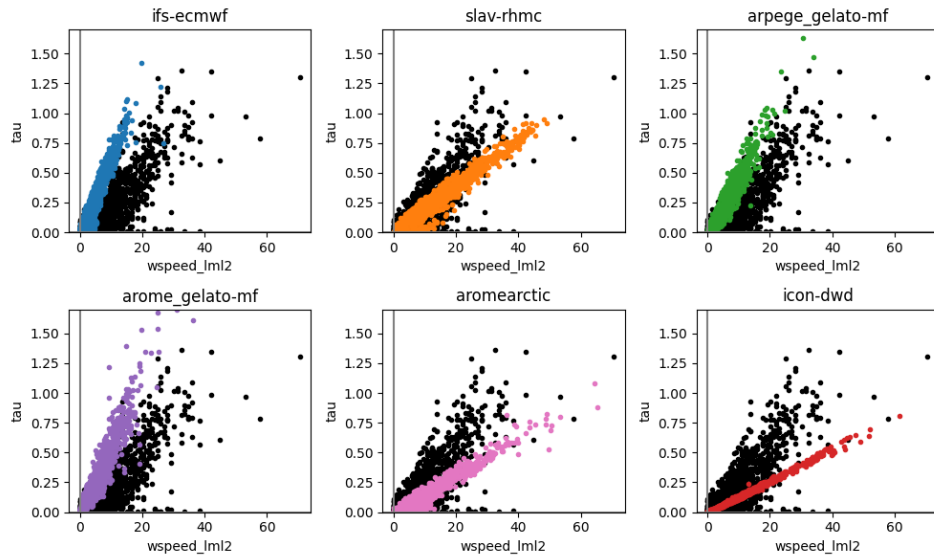
Deleted: 1

Deleted: 2

Deleted: 1

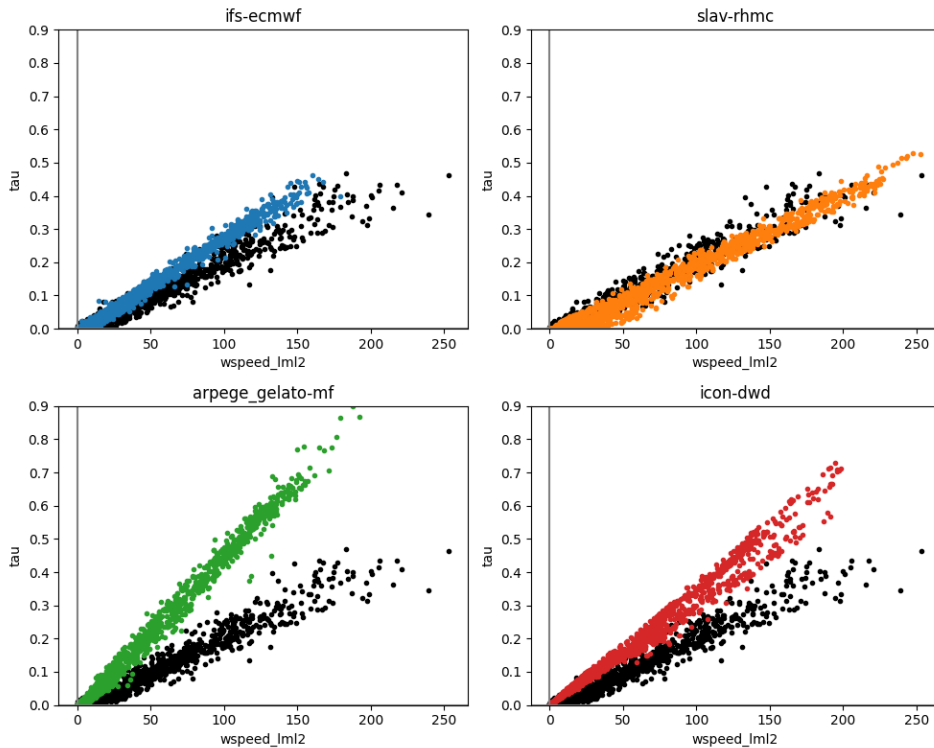
Deleted: also

Deleted: 2



683  
 684 **Figure 13:** scatter plots of wind stress vs. the square of the near-surface (lowest model level) wind speed at Sodankylä.  
 685 The observed points are shown in black and hourly values during the second day of the forecast forecast is shown in  
 686 colours.  
 687

**Deleted: 1**



689  
690 **Figure 14:** as Figure 13, but for Utqiāgvik.  
691  
692

**Deleted:** 2

**Deleted:** 1

	Sodankylä	Utqiāgvik
Obs	1.62	0.0012
IFS	1.83 (1.83-1.83)	0.00130 (0.00130-0.00130)
ARPEGE	1.50 (1.49-1.51)	0.00884 (0.00880-0.00891)
SLAV	1.60 (1.59-1.61)	0.00135 (0.00129-0.00144)
ICON-DWD	0.20 (0.20-0.41)	0.00700 (0.00151-0.00981)
AROME-Arctic	0.45 (0.45-0.45)	Outside model domain

**Deleted:** 2

**Deleted:** 53

693 **Table 4. Roughness lengths for momentum (m) at Sodankylä and Utqiāgvik from observations and models. For the**  
694 **models the mean is stated and the range of values is stated in parenthesis.**

**Deleted:** 3

**Deleted:** 4

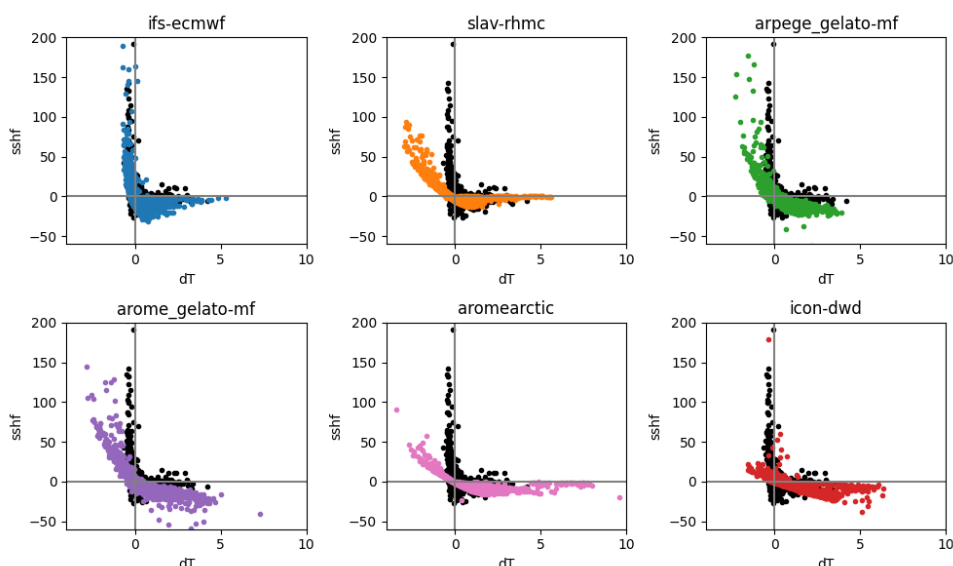
**Deleted:** The basic shape of the observed points is the same at both sites, but with fewer cases of instability at Utqiāgvik compared to Sodankylä. ...

**Deleted:** -GELATO

695 The scatterplots for the sensible heat flux (Figures 15, 16) also provide some insights into the differences in the process  
696 representation between the models. All the models capture the link between the SHF and the temperature gradient dictated by  
697 M-O theory (see Eqn 3) however, the shape of the relationship varies between the models. For example, for the ARPEGE and  
698 AROME-MF models the sign of the sensible heat flux does not change in a binary way with  $\Delta T$ , there is spread in the location  
699 along the x-axis where this occurs. This could be due to differences in the numerical formulation of the models, i.e. the timestep  
700 at which the flux and temperature terms are stored or due to the fact that we are looking at the gridbox mean values where the  
701 fluxes are aggregated from values computed on different surface tiles. At Sodankylä, the IFS, SLAV and AROME-ARCTIC

712 model have a clear tapering in the scaled sensible heat flux towards zero for high values of  $\Delta T$ . However, the AROME-MF,  
 713 ARPEGE and ICON do not have such a tapering and the scaled heat flux continues to grow with larger  $\Delta T$ , which is  
 714 qualitatively inconsistent with the observations and will lead to higher fluxes in very stable conditions inhibiting cooling of  
 715 the surface. There is also a clear difference in the range of  $\Delta T$  between the different models however, in the models this is an  
 716 aggregate of different surface types representing forest canopy top, bare snow and frozen water and because we do not have a  
 717 trustable observation of the temperature of the top of the canopy frozen water during freezing conditions it is not clear what  
 718 the realistic range should be. Note also that the SHF at Sodankylä is measured at 24.5 m and for process consistency  $\Delta T$  is  
 719 calculated using the air temperatures observed at 18m and 32m which is not directly comparable with the models.

720  
 721 Except for ICON, differences between the models at Utqiágvik are less pronounced. IFS, SLAV and ARPEGE have quite a  
 722 similar shape, and all underestimate the magnitude of the scaled heat flux for low values of  $\Delta T$ , potentially due to the slow bias  
 723 in wind speeds near to the surface. Note that the large values of  $\Delta T$  for the SLAV model are because the lowest model level is  
 724 at  $\sim 30$ m, compared to  $\sim 10$ m for the other models. Note that the ICON model has a large fraction of open ocean in the grid cell  
 725 considered and, therefore the model tends to be biased towards convective conditions (i.e. most points are in the top left  
 726 quadrant of Figure 16 where the sensible heat flux is heating the atmosphere), this is likely the main reason for the warm bias  
 727 in surface skin-temperature and 2m-air temperature. For the other models shown in Figure 16, the grid-point considered is  
 728 100% land.



731  
 732 **Figure 15:** scatter plots of the scaled sensible heat flux (SHF/U) vs. thermal stratification,  $\Delta T = T_{lmf} - T_{skin}$ , at Sodankylä.  
 733 The observed points are shown in black and hourly values during the second day of the forecasts are shown in colours.  
 734 Note that at Sodankylä the SHF is measured at 24.5 m and for process consistency  $\Delta T$  is calculated using the  
 735 temperatures observed at 18m and 32m so is not directly comparable with the models which use the skin temperature,  
 736  $T_{skin}$ , and the lowest model level,  $T_{lmf}$ .

**Deleted:** , which has a large fraction of open ocean in the grid cell and therefore are biased towards convective conditions

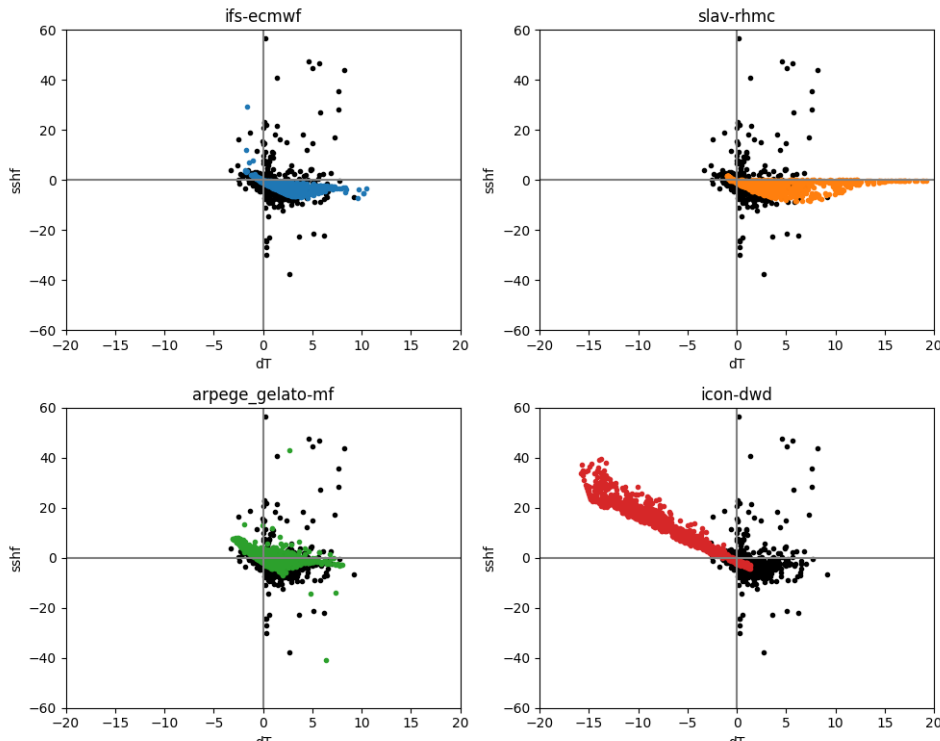
**Deleted:** is

**Deleted:** 3

**Formatted:** Subscript

**Formatted:** Font: Italic

**Formatted:** Font: Italic, Subscript



742  
 743 **Figure 16:** as Figure 15 but for Utqiagvik. Note that for the observations  $\Delta T$  is calculated using the 10m air temperature  
 744 and an estimate of the surface temperature from an infrared sensor.

**Deleted:** 4

**Deleted:** 3

745 **4. Conclusions and future plans**

746 In this manuscript we have outlined the motivation for YOPPsiteMIP, documented the current status of the YOPPsiteMIP  
 747 forecast [MMDF](#) data archived on the YOPP data portal (hosted by MET Norway), and presented some multi-model forecast  
 748 evaluation examples to demonstrate the utility of the MMDFs and MODFs using data from the YOPP SOP1, which occurred  
 749 during February and March 2018. The main conclusions from this analysis are that:

- 750 • Near-surface temperature and wind speed forecast errors vary considerably between the different sites, reflecting both  
 751 a range of climate conditions and forecast performance across the [selected](#) sites.
- 752 • A common feature of several sites, namely Sodankylä, Barrow, Tiksi, Eureka, is a [warm](#) bias during periods of  
 753 extreme cold which goes hand-[in-hand](#) with a lack of temperature variability in the lowest ~100m of the atmosphere.
- 754 • This lack of variability is investigated further at Utqiagvik, Tiksi and Sodankylä where radiation components were  
 755 observed and provided [in the MODFs and MMDFs](#), which enabled us to investigate the sensitivity of T2m to radiative  
 756 forcing:

**Deleted:** geographies represented by this selection of

**Deleted:** conditional

**Deleted:** in hand

764           ○ At all three sites the models tend to underestimate the sensitivity of T2m and the surface skin temperature  
 765           (or  $LW\uparrow$ ) to variations in radiative forcing and do not capture extreme minima in these variables, although  
 766           the AROME-Arctic and CAPS models perform better in this regard.

767           ● At Utqiagvik and Sodankylä, since turbulent fluxes were provided in addition, we were able to investigate the link  
 768           between these fluxes and the bulk parameters. This highlighted:

769           ○ Differences in the parameterisation of turbulent fluxes, particularly the specification of the roughness length  
 770           for momentum which varies by a little less than an order of magnitude between different models.

771           ○ The high importance of the ground heat flux, particularly at the Utqiagvik and Tiksi sites, where stable  
 772           conditions dominate. Note that despite this importance, this flux is not observed at these two sites.

**Deleted:** the thermal representation of the land surface as an issue with all forecasts, likely due to the single-layer representation of snow used in all the forecasts submitted to YOPPsiteMIP but potentially also due to the thermal representation of forest canopy at Sodankylä.

**Deleted:** 1

773           Process studies which compare point observations to gridded model output, need to be carried out in awareness of sub-tile  
 774           representativeness issues. For fine resolution models it is always recommended to provide output from multiple grid-points (as  
 775           in this study), centred on the observatory, to be able to pair land-based observations to a model tile with dominant land-cover.  
 776           For coarse resolution models, we recommend to provide variables for the different sub-tile components (bare soil, vegetation,  
 777           water, ice, ...). The more the site characteristics are matched to the correct model output, the more reliable diagnosis on the  
 778           model capability to reproduce the observed physical process. In this study we found that the land-ocean contrast in the Arctic  
 779           in winter does not significantly affect the surface energy budget sensitivity to radiative forcing in the CAPS model (in Section  
 780           3.4, the ocean-dominated Utqiagvik grid-points of CAPS do not stand out with respect to the other models), because the frozen  
 781           ocean has similar characteristics to the snow-covered land surface. On the other hand, the ICON model, which has very low  
 782           sea ice values (~10%) has much warmer temperatures than the other models at Utqiagvik, and as a result the sensible heat  
 783           flux behaves differently compared to the other models. Accounting for the land-ocean contrast will be crucial in the sea-ice  
 784           free summer SOP2 period that will be evaluated in the future.

**Deleted:** and ICON

**Deleted:** acts as

**Deleted:** the wind stress and sensible heat flux are affected by the ocean-vs-land tile characteristics (

**Deleted:** in Section 3.5, ICON

**Deleted:** with respect

785           The development of the MODFs and MMDFs is ongoing and will be completed in phases. The initial phase was to collect  
 786           basic meteorology data and the main components of the radiation budget. Work on this initial phase is completed and the next  
 787           phase will provide a wider range of parameters (e.g. turbulent fluxes and cloud parameters) included in the MODFs. This is a  
 788           more complicated, but very necessary step since the models differ significantly in terms of surface heat and momentum fluxes  
 789           as well as cloud properties (not shown). There are also plans to extend the MODF and MMDF concept to Antarctica, focussing  
 790           on the Southern-hemisphere SOPs. These future phases of the YOPPsiteMIP will allow more detailed studies on e.g.:

**Deleted:** hugely

**Deleted:** stable boundary layers, diurnal cycles and surface exchange processes,

**Deleted:** 1

**Deleted:** radiative forcing and albedo

**Deleted:** 1

**Deleted:** vertical structure of the lower atmosphere,

**Deleted:** 1

**Deleted:** assessment of cloud

**Deleted:** hydrometeors

**Deleted:** Morris

**Deleted:** 3

**Deleted:**

**Deleted:** available on gitlab and details can be found in Gallagher et al. (manuscript in preparation)

## 802           Appendix A: Table of acronyms

803           EDMF=Eddy Diffusivity Mass Flux.

804           FE=Finite Element,

832 FD=Finite Difference,  
833 FV=Finite Volume,  
834 H=Hydrostatic,  
835 HARATU = HARMONIE-AROME with RACMO Turbulence  
836 HTESSEL=Hydrology-Tiled ECMWF Scheme for Surface Exchanges over Land,  
837 ICE3 = Three-class ice parameterization  
838 IQR = Inter-Quartile Range  
839 ISBA= Interactions between Surface–Biosphere–Atmosphere,  
840 NH=Non-hydrostatic,  
841 SURFEX = Surface Externalisée,  
842 TERRA = Land Surface module of the ICON weather forecast model.  
843 TKE=Turbulent Kinetic Energy,

844 **Data availability statement**

845 All MMDF and MODFs are available on the YOPP Data Portal (<https://yopp.met.no>), hosted by the Norwegian Meteorological  
846 Institute, for perpetuity (ie. longer than 10 years). The YOPP Data Portal is relying on the Arctic Data Centre  
847 (<https://adc.met.no>) for data stewarding and the YOPPSiteMIP data can be programmatically accessed using the machine  
848 interface for the Arctic Data Centre or can be accessed directly from  
849 [https://thredds.met.no/thredds/catalog/alertness/YOPP\\_supersite](https://thredds.met.no/thredds/catalog/alertness/YOPP_supersite) /obs/catalog.html, for the MODFs and  
850 <https://thredds.met.no/thredds/catalog/YOPPSiteMIP-models/catalog.html>, for the MMDFs.

851

852 The SOP1 and SOP2 MODFs for each station shown in white in Fig 1 has been assigned a separate DOI, as described in  
853 [Mariani et al. \(2024\)](#). In the case of the MMDFs a DOI is assigned to the data for each forecast model:

- 854 • ECMWF-IFS: <https://doi.org/10.21343/A6KA-7142>,
- 855 • ARPEGE-MF: <https://doi.org/10.21343/T31Z-J391>,
- 856 • SLAV-RHMC: <https://doi.org/10.21343/J4SJ-4N61>
- 857 • DWD-ICON: <https://doi.org/10.21343/09KM-BJ07>,
- 858 • ECCC-CAPS: <https://doi.org/10.21343/2BX6-6027>,
- 859 • AROME-MF: <https://doi.org/10.21343/JZH3-2470>,
- 860 • AROME-Arctic: <https://doi.org/10.21343/47AX-MY36>.

**Deleted:** Morris

**Deleted:** submitted

**Formatted:** Font colour: Auto

862 **Code availability statement**

863 Apart from the ECMWF-IFS, for which an open access version of the code is available here:  
864 <https://confluence.ecmwf.int/display/OIFS>, the model codes are not open access.

**Formatted:** No bullets or numbering

866 **Funding**

- 867 • JD was supported by European Union's Horizon 2020 Research and Innovation program through Grant Agreement  
868 871120 (INTERACTIII).
- 869 • MT was partially supported with Russian Science Foundation, Grant 21-17-00254
- 870 • RP was supported by European Union's Horizon 2020 Research and Innovation program through Grant Agreement  
871 101003590 (PolarRES)

874 • TR was supported by the Norwegian Research Council project no. 280573 'Advanced models and weather prediction  
875 in the Arctic: enhanced capacity from observations and polar process representations (ALERTNESS)'  
876

877 **Author contributions**

878 The initial YOPPsiteMIP, MODF and MMDF concepts were developed by GS, JD, BC, TU, SK, LMH, AS and EB. JD, BC,  
879 EB, NA, HF, TR, RF & MT produced or ran simulations to make MMDFs. TU, EA, MG, LXH, JH, ZM, SM, EO, IS, MG, JT  
880 and RP produced or were involved in the production of MODFs. LF, MD and ØG were responsible for the YOPPsiteMIP  
881 archive hosted at MET Norway. JD produced the figures and wrote the manuscript with comments and input from all co-  
882 authors.  
883

884 **Competing Interests**

885 The authors declare that they have no conflict of interest.  
886

887 **Acknowledgements**

888 This is a contribution to the Year of Polar Prediction (YOPP), a flagship activity of the Polar Prediction Project (PPP), initiated  
889 by the World Weather Research Programme (WWRP) of the World Meteorological Organisation (WMO). We acknowledge  
890 the WMO WWRP for its role in coordinating this international research activity. We would specifically like to thank Thomas  
891 Jung, Jeff Wilson and wider PPP steering group for their tireless support of YOPPsiteMIP.

892 **References**

893 Arduini, G., Balsamo, G., Dutra, E., Day, J. J., Sandu, I., Boussetta, S., & Haiden, T. (2019). Impact of a multi-layer snow  
894 scheme on near-surface weather forecasts. *Journal of Advances in Modeling Earth Systems*, 11, 4687– 4710.  
895 <https://doi.org/10.1029/2019MS001725>

896 Akish, E., & Morris, S. (2023a). MODF for Eureka, Canada, during YOPP SOP1 and SOP2. Norwegian Meteorological  
897 Institute. <https://doi.org/10.21343/R85J-TC61>

898 Akish, E., & Morris, S. (2023b). MODF for Tiksi, Russia, during YOPP SOP1 and SOP2. Norwegian Meteorological Institute.  
899 <https://doi.org/10.21343/5BWN-W881>

900 Akish, E., & Morris, S. (2023c). MODF for Utqiagvik, Alaska, during YOPP SOP1 and SOP2. Norwegian Meteorological  
901 Institute. <https://doi.org/10.21343/A2DX-NQ55>

902 Atlaskin, E. and Vihma, T.: Evaluation of NWP results for wintertime nocturnal boundary-layer temperatures over Europe and  
903 Finland, *Q. J. R. Meteorol. Soc.*, 138, 1440–1451, <https://doi.org/10.1002/qj.1885>, 2012.

904 Baines, P. G., & Palmer, T. N. (1990). Rationale for a new physically-based parametrisation of sub-grid scale orographic  
905 effects. *Tech. Rep. 169*, European Centre for Medium-Range Weather Forecasts, Reading, UK.

906 Baldauf, M., Seifert, A., Förstner, J., Majewski, D., Raschendorfer, M., & Reinhardt, T.: Operational Convective-Scale  
907 Numerical Weather Prediction with the COSMO Model: Description and Sensitivities, *Monthly Weather Review*, 139(12),  
908 3887–3905, 2011.

909 Balsamo, G., Beljaars, A., Scipal, K., Viterbo, P., van den Hurk, B., Hirschi, M., and Betts, A. K.: A Revised Hydrology for  
910 the ECMWF Model: Verification from Field Site to Terrestrial Water Storage and Impact in the Integrated Forecast System,  
911 *J. Hydrometeorol.*, 10, 623–643, <https://doi.org/10.1175/2008JHM1068.1>, 2009.

912 Batrak, Y. and Müller, M.: On the warm bias in atmospheric reanalyses induced by the missing snow over Arctic sea-ice, *Nat.*  
913 *Commun.*, 10, 1–8, <https://doi.org/10.1038/s41467-019-11975-3>, 2019.

914 Bauer, P., Magnusson, L., Thépaut, J.-N., and Hamill, T. M.: Aspects of ECMWF model performance in polar areas, *Q. J. R.*  
915 *Meteorol. Soc.*, 142, 583–596, <https://doi.org/10.1002/qj.2449>, 2016.

Deleted: 1

917 Bazile, E., & Azouz, N. (2023a). Merged model Data Files (MMDFs) for the Meteo France ARPEGE global forecast model  
 918 for various Polar sites. Norwegian Meteorological Institute. <https://doi.org/10.21343/T31Z-J391>

919 Bazile, E., & Azouz, N. (2023b). MMDFs for the Meteo France AROME regional forecast model for various Arctic sites.  
 920 Norwegian Meteorological Institute. <https://doi.org/10.21343/JZH3-2470>

921 E.Bazile, N. Azouz, A. Napoly, C. Loo: Impact of the 1D sea-ice model GELATO in the global model ARPEGE. France  
 922 6-03. [http://bluebook.meteoinfo.ru/index.php?year=2020&ch\\_=2](http://bluebook.meteoinfo.ru/index.php?year=2020&ch_=2)

923 Bazile, E., Marquet, P., Bouteloup, Y., and Bouyssel, F.: The Turbulent Kinetic Energy (TKE) scheme in the NWP models at  
 924 Météo-France, ECMWF GABLS Workshop on Diurnal cycles and the stable boundary layer, 7-10 November 2011.

925 Bélair, S., Brown, R., Mailhot, J., Bilodeau, B., & Crevier, L. (2003). Operational Implementation of the ISBA Land Surface  
 926 Scheme in the Canadian Regional Weather Forecast Model. Part II: Cold Season Results, *Journal of Hydrometeorology*, 4(2),  
 927 371-386.

928 Bélair, S., J. Mailhot, C. Girard, and P. Vaillancourt, 2005: Boundary Layer and Shallow Cumulus Clouds in a Medium-Range  
 929 Forecast of a Large-Scale Weather System. *Mon. Wea. Rev.*, 133, 1938–1960, <https://doi.org/10.1175/MWR2958.1>.

930 Beljaars, A. C. M. and Holtslag, A. a. M.: Flux Parameterization over Land Surfaces for Atmospheric Models, *J. Appl.*  
 931 *Meteorol.*, 30, 327–341, [https://doi.org/10.1175/1520-0450\(1991\)030<0327:FPOLSF>2.0.CO;2](https://doi.org/10.1175/1520-0450(1991)030<0327:FPOLSF>2.0.CO;2), 1991.

932 Bengtsson, L., Andrae, U., Aspelin, T., Batrak, Y., Calvo, J., Rooy, W. de, Gleeson, E., Hansen-Sass, B., Homleid, M., Hortal,  
 933 M., Ivarsson, K.-I., Lenderink, G., Niemelä, S., Nielsen, K. P., Onvlee, J., Rontu, L., Samuelsson, P., Muñoz, D. S., Subias,  
 934 A., Tijm, S., Toll, V., Yang, X., and Køltzow, M. Ø.: The HARMONIE–AROME Model Configuration in the ALADIN–  
 935 HRLAM NWP System, *Mon. Weather Rev.*, 145, 1919–1935, <https://doi.org/10.1175/MWR-D-16-0417.1>, 2017.

936 Bechtold, P., M. Köhler, T. Jung, F. Doblas-Reyes, M. Leutbecher, M. J. Rodwell, F. Vitart, and G. Balsamo, 2008: Advances  
 937 in simulating atmospheric variability with the ECMWF model: From synoptic to decadal time-scales. *Quarterly Journal of the*  
 938 *Royal Meteorological Society*, 134 (634), 1337–1351, <https://doi.org/10.1002/qj.289>, URL  
 939 <https://onlinelibrary.wiley.com/doi/10.1002/qj.289>.

940 Bechtold, P., E. Bazile, F. Guichard, P. Mascart and E. Richard, 2001 : A mass flux convection scheme for regional and global  
 941 models. *Quart. J. Roy. Meteor. Soc.*, 127, 869–886.

942 Bougeault, P.: Cloud ensemble relations for use in higher order models of the planetary boundary layer, *J. Atmos. Sci.*, 39,  
 943 2691–2700, 1982.

944 Bougeault, P. (1985). A simple parameterisation of the large scale effects of cumulus convection. *Mon. Wea. Rev.*, 4:469–485.

945 Bromwich, D. H., Werner, K., Casati, B., Powers, J. G., Gorodetskaya, I. V., Massonnet, F., Vitale, V., Heinrich, V. J., Liggett,  
 946 D., Arndt, S., Barja, B., Bazile, E., Carpentier, S., Carrasco, J. F., Choi, T., Choi, Y., Colwell, S. R., Cordero, R. R., Gervasi,  
 947 M., Haiden, T., Hirasawa, N., Inoue, J., Jung, T., Kalesse, H., Kim, S.-J., Lazzara, M. A., Manning, K. W., Norris, K., Park,  
 948 S.-J., Reid, P., Rigor, I., Rowe, P. M., Schmittlißen, H., Seifert, P., Sun, Q., Uttal, T., Zannoni, M., and Zou, X.: The Year of  
 949 Polar Prediction in the Southern Hemisphere (YOPP-SH), *Bull. Am. Meteorol. Soc.*, 101, E1653–E1676,  
 950 <https://doi.org/10.1175/BAMS-D-19-0255.1>, 2020.

951 Buizza, R., Bidlot, J.-R., Janousek, M., Keeley, S., Mogensen, K., and Richardson, D.: New IFS cycle brings sea-ice coupling  
 952 and higher ocean resolution, *ECMWF Newsl.* - Number 150, 14–17, <https://doi.org/10.21957/xb0v3ybily>, 2017.

953 Casati, B. (2023). MMDFs for the Environment and Climate Change Canada-CAPS regional forecast model for various Arctic  
 954 sites. Norwegian Meteorological Institute. <https://doi.org/10.21343/2BX6-6027>

955 Casati, B., T. Robinson, F. Lemay, M. Køltzow, T. Haiden, E. Mekis, F. Lespinas, V. Fortin, G. Gascon, J. Milbrandt, G.  
 956 Smith (2023) Performance of the Canadian Arctic Prediction System during the YOPP Special Observing Periods.  
 957 Atmosphere-Ocean, <https://doi.org/10.1080/07055900.2023.2191831>

958 Casati, B.: Model process-based evaluation using high-frequency multi-variate observations at the Arctic and Antarctic  
 959 supersites during the Year of Polar Prediction: the YOPPSiteMIP, n.d.

**Deleted: 1**

**Deleted: 1**

**Deleted:** Bélair, S., Brown, R., Mailhot, J., Bilodeau, B., & Crevier, L. (2003). Operational Implementation of the ISBA Land Surface Scheme in the Canadian Regional Weather Forecast Model. Part II: Cold Season Results, *Journal of Hydrometeorology*, 4(2), 371-386.

**Deleted: 1**

**Deleted:** Belair et al., 2005: Boundary Layer and Shallow Cumulus Clouds in a Medium-Range Forecast of a Large-Scale Weather System. *Monthly Weather Review*, Vol. 133, 1938–1960

**Deleted: 1**

972 Catry, B., Geleyn, J. F., Bouyssel, F., Cedilnik, J., Brožková, R., & Derková, M. (2008). A new sub-grid scale lift formulation  
973 in a mountain drag parameterisation scheme. *Meteorologische Zeitschrift*, 17(2), 193–208. <https://doi.org/10.1127/0941-2948/2008/0272>

974 Cheng, Y., V. M. Canuto, and A. M. Howard, 2002: An Improved Model for the Turbulent PBL. *J. Atmos. Sci.*, 59, 1550–  
975 1565, [https://doi.org/10.1175/1520-0469\(2002\)059<1550:AIMFTT>2.0.CO;2](https://doi.org/10.1175/1520-0469(2002)059<1550:AIMFTT>2.0.CO;2).

976 Coté, J.-S., Gravel, A., Méthot, A., Patoine, M., Roch, and A. Staniforth, 1998: The operational CMC–MRD Global  
977 Environmental Multiscale (GEM) model. Part I: Design considerations and formulation. *Mon. Wea. Rev.*, 126, 1373–1395,  
978 doi:10.1175/1520-0493(1998)126,1373:TOCMGE.2.0.CO;2.

979 **Cuxart, J., Bougeault, P. and Redelsperger, J.-L. (2000), A turbulence scheme allowing for mesoscale and large-eddy**  
980 **simulations. Q.J.R. Meteorol. Soc.**, 126: 1-30. <https://doi.org/10.1002/qj.49712656202>

981 Cuxart, J., Holtslag, A. A. M., Beare, R. J., Bazile, E., Beljaars, A., Cheng, A., Conangla, L., Ek, M., Freedman, F., Hamdi,  
982 R., Kerstein, A., Kitagawa, H., Lenderink, G., Lewellen, D., Mailhot, J., Mauritsen, T., Perov, V., Schayes, G., Steeneveld,  
983 G.-J., Svensson, G., Taylor, P., Weng, W., Wunsch, S., and Xu, K.-M.: Single-Column Model Intercomparison for a Stably  
984 Stratified Atmospheric Boundary Layer, *Boundary-Layer Meteorol.*, 118, 273–303, <https://doi.org/10.1007/s10546-005-3780-1>, 2006.

985 Day, J. (2023). MMDFs for the ECMWF-IFS global forecast model for various Polar sites. Norwegian Meteorological  
986 Institute. <https://doi.org/10.21343/A6KA-7142>

987 Day, J. J., Sandu, I., Magnusson, L., Rodwell, M. J., Lawrence, H., Bormann, N., and Jung, T.: Increased Arctic influence on  
988 the midlatitude flow during Scandinavian Blocking episodes, *Q. J. R. Meteorol. Soc.*, 145, 3846–3862,  
989 doi:10.1002/qj.3673, 2019.

990 Day, J. J., Arduini, G., Sandu, I., Magnusson, L., Beljaars, A., Balsamo, G., Rodwell, M., and Richardson, D.: Measuring the  
991 Impact of a New Snow Model Using Surface Energy Budget Process Relationships, *J. Adv. Model. Earth Syst.*, 12,  
992 doi:10.1029/2020MS002144, 2020.

993 Day, J. J., Keeley, S., Arduini, G., Magnusson, L., Mogensen, K., Rodwell, M., Sandu, I., and Tietsche, S.: Benefits and  
994 challenges of dynamic sea ice for weather forecasts, *Weather Clim. Dyn.*, 3, 713–731, <https://doi.org/10.5194/wcd-3-713-2022>, 2022.

995 Delage, Y. (1997): Parametrizing sub-grid scale vertical transport in atmospheric models under statically stable  
996 conditions. *Boundary-Layer Meteorology* 82, 23–48 (1997). <https://doi.org/10.1023/A:1000132524077>

997 Delage, Y., and C. Girard (1992): Stability functions correct at the free convection limit and consistent for both the surface  
1000 and Ekman layers. *Boundary-Layer Meteorol.* 58, 19–31. <https://doi.org/10.1007/BF00120749>

1001 Donlon, C. J., Martin, M., Stark, J., Roberts-Jones, J., Fiedler, E., and Wimmer, W.: The Operational Sea Surface Temperature  
1002 and Sea Ice Analysis (OSTIA) system, *Remote Sens. Environ.*, 116, 140–158, <https://doi.org/10.1016/j.rse.2010.10.017>, 2012.

1003 **Bašták-Ďurán, I. B., J. Geleyn, F. Váňa, J. Schmidli, and R. Brožková, 2018: A Turbulence Scheme with Two Prognostic**  
1004 **Turbulence Energies. *J. Atmos. Sci.*, 75**, 3381–3402, <https://doi.org/10.1175/JAS-D-18-0026.1>.

1005 Dyer, A. J. (1974). A review of flux-profile relationships. *Boundary-Layer Meteorol.*, 7, 363–372.

1006

1007

1008 Emmerson, C., and G. Lahn, 2012: Arctic opening: Opportunity and risk in the high north. *Lloyds Rep.*, 59 pp. [Available  
1009 online at [www.chathamhouse.org/sites/files/chathamhouse/public/Research/Energy,%20Environment%20and%20Development/0412arctic.pdf](http://www.chathamhouse.org/sites/files/chathamhouse/public/Research/Energy,%20Environment%20and%20Development/0412arctic.pdf).]

1010

1011 Forbes, R. M. and Ahlgrimm, M.: On the Representation of High-Latitude Boundary Layer Mixed-Phase Cloud in the ECMWF  
1012 Global Model, *Mon. Weather Rev.*, 142, 3425–3445, <https://doi.org/10.1175/MWR-D-13-00325.1>, 2014.

1013 Frank, H. (2023). MMDFs for the DWD-ICON global forecast model for various Arctic sites. Norwegian Meteorological  
1014 Institute. <https://doi.org/10.21343/09KM-BJ07>

**Deleted:** Curry, J.: On the Formation of Continental Polar Air, *J. Atmospheric Sci.*, 40, 2278–2292, [https://doi.org/10.1175/1520-0469\(1983\)040<2278:OTFOCP>2.0.CO;2](https://doi.org/10.1175/1520-0469(1983)040<2278:OTFOCP>2.0.CO;2), 1983.

**Deleted:** 1

1019 Gerard, L. and Geleyn, J.-F. (2005), Evolution of a subgrid deep convection parametrization in a limited-area model with  
 1020 increasing resolution. *Q.J.R. Meteorol. Soc.*, 131: 2293–2312. <https://doi.org/10.1256/qj.04.72>

1021 Gerard, L., J. Piriou, R. Brožková, J. Geleyn, and D. Banciu, 2009: Cloud and Precipitation Parameterization in a Meso-  
 1022 Gamma-Scale Operational Weather Prediction Model. *Mon. Wea. Rev.*, 137, 3960–  
 1023 3977, <https://doi.org/10.1175/2009MWR2750.1>.

1024 Girard, C., and Coauthors, 2014: Staggered vertical discretization of the Canadian Environmental Multiscale (GEM) model  
 1025 using a coordinate of the log-hydrostatic-pressure type. *Mon. Wea. Rev.*, 142, 1183–1196, doi:10.1175/MWR-D-13-00255.1.

1026 Goessling, H. F., and Coauthors, 2016: Paving the way for the Year of Polar Prediction. *Bull. Amer. Meteor. Soc.*, 97, ES85–  
 1027 ES88, doi:10.1175/BAMS-D-15-00270.1.

1028 Haiden, T., Sandu, I., Balsamo, G., Arduini, G., and Beljaars, A.: Addressing biases in near-surface forecasts, ECMWF,  
 1029 <https://doi.org/10.21957/eng71d53th>, 2018.

1030 Hartten, L. M. and Khalsa, S. J. S.: The H-K Variable SchemaTable developed for the YOPPSiteMIP,  
 1031 <https://doi.org/10.5281/zenodo.6463464>, 2022.

1032 Heise E., Ritter B. & Schrodin R. 2006. Operational implementa- tion of the multilayer soil model. COSMO Technical Reports  
 1033 No. 9. Offenbach am Main, Germany: Consortium for Small-Scale Modelling.

1034 Hogan, R. J. and Bozzo, A.: A Flexible and Efficient Radiation Scheme for the ECMWF Model, *J. Adv. Model. Earth Syst.*,  
 1035 10, 1990–2008, <https://doi.org/10.1029/2018MS001364>, 2018.

1036 Högström, U. (1988). Non-dimensional wind and temperature profiles in the atmospheric surface layer: A re-evaluation.  
 1037 *Boundary-Layer Meteorol.*, 42, 55–78.

1038 Holt, J. (2023). Merged Observatory Data File (MODF) for Ny Alesund. Norwegian Meteorological Institute.  
 1039 <https://doi.org/10.21343/Y89M-6393>

1040 Holtslag, A. A. M., & De Bruin, H. A. R. (1988). Applied Modeling of the Nighttime Surface Energy Balance over Land,  
 1041 *Journal of Applied Meteorology and Climatology*, 27(6), 689–704.

1042 Holtslag, A. A. M., Svensson, G., Baas, P., Basu, S., Beare, B., Beljaars, A. C. M., Bosveld, F. C., Cuxart, J., Lindvall, J.,  
 1043 Steeneveld, G. J., Tjernström, M., & Van De Wiel, B. J. H. (2013). Stable Atmospheric Boundary Layers and Diurnal Cycles:  
 1044 Challenges for Weather and Climate Models, *Bulletin of the American Meteorological Society*, 94(11), 1691–1706.

1045 Huang, L., Mariani, Z., & Crawford, R. (2023a). MODF for Iqaluit Airport, Iqaluit, Nunavut, Canada during YOPP SOP1 and  
 1046 SOP2. Norwegian Meteorological Institute. <https://doi.org/10.21343/YRNF-CK57>

1047 Huang, L., Mariani, Z., & Crawford, R. (2023b). MODF for Erik Nielsen Airport, Whitehorse, Canada during YOPP SOP1  
 1048 and SOP2. Norwegian Meteorological Institute. <https://doi.org/10.21343/A33E-J150>

1049 Iacono, M., Delamere, J., Mlawer, E., Shephard, M., Clough, S. and Collins, W. (2008). Radiative forcing by long-lived  
 1050 greenhouse gases: Calculations with the AER radiative transfer models. *J. Geophys. Res.*, 113D, 13103.

1051 Ingleby, B., Arduini, G., Balsamo, G., Bousseta, S., Ochi, K., Pinnington, E., and De Rosnay, P.: Improved two-metre-  
 1052 temperature forecasts in the 2024 upgrade, *ECMWF Newsletter - Number 178*, 2024.

1053 Jung, T. and Matsueda, M. (2016). Verification of global numerical weather forecasting systems in polar regions using TIGGE  
 1054 data. *Q.J.R. Meteorol. Soc.*, 142: 574–582. <https://doi.org/10.1002/qj.2437>

1055 Jung, T., Gordon, N. D., Bauer, P., Bromwich, D. H., Chevallier, M., Day, J. J., Dawson, J., Doblas-Reyes, F., Fairall, C.,  
 1056 Goessling, H. F., Holland, M., Inoue, J., Iversen, T., Klebe, S., Lemke, P., Losch, M., Makshtas, A., Mills, B., Nurmi, P.,  
 1057 Perovich, D., Reid, P., Renfrew, I. A., Smith, G., Svensson, G., Tolstykh, M., and Yang, Q.: Advancing Polar Prediction  
 1058 Capabilities on Daily to Seasonal Time Scales, *Bull. Am. Meteorol. Soc.*, 97, 1631–1647, <https://doi.org/10.1175/BAMS-D-14-00246.1>, 2016.

1059

1060 Kain, J. S., and J. M. Fritsch, 1990: A One-Dimensional Entraining/Detraining Plume Model and Its Application in Convective  
 1061 Parameterization. *J. Atmos. Sci.*, 47, 2784–2802, [https://doi.org/10.1175/1520-0469\(1990\)047<2784:AODEPM>2.0.CO;2](https://doi.org/10.1175/1520-0469(1990)047<2784:AODEPM>2.0.CO;2).

**Deleted:** Iacono, M., Delamere, J., Mlawer, E., Shephard, M., Clough, S. and Collins, W. (2008). Radiative forcing by long-lived greenhouse gases: Calculations with the AER radiative transfer models. *J. Geophys. Res.*, 113D, 13103.

**Deleted:** 1

**Deleted:** 1

**Deleted:** Illingworth, A. J., Hogan, R. J., O'Connor, E. j., Bouniol, D., Brooks, M. E., Delan  , J., Donovan, D. P., Eastment, J. D., Gassiat, N., Goddard, J. W. F., Haeffelin, M., Baltink, H. K., Krasnov, O. A., Pelon, J., Piriou, J.-M., Protat, A., Russchenberg, H. W. J., Seifert, A., Tompkins, A. M., van Zadelhoff, G.-J., Vinit, F., Willen, U., Wilson, D. R., and Wrench, C. L.: Cloudnet, *Bull. Am. Meteorol. Soc.*, 88, 883–898, <https://doi.org/10.1175/BAMS-88-6-883>, 2007.

**Formatted:** Space After: 0 pt, Line spacing: 1.5 lines

**Formatted:** Space After: 0 pt, Line spacing: 1.5 lines

1076 [Kähnert, M., Sodemann, H., Remes, T.M. et al. Spatial Variability of Nocturnal Stability Regimes in an Operational Weather](#)  
 1077 [Prediction Model. Boundary-Layer Meteorol 186, 373–397 \(2023\). https://doi.org/10.1007/s10546-022-00762-1](#)

1078 Karlsson J. and G. Svensson, 2013: Consequences of poor representation of Arctic sea-ice albedo and cloud-radiation  
 1079 interactions in the CMIP5 model ensemble. *Geophys. Res. Lett.*, 40, 4374–4379, doi:10.1002/grl.50768

1080 Køltzow, M., Casati, B., Bazile, E., Haiden, T., and Valkonen, T.: An NWP Model Intercomparison of Surface Weather  
 1081 Parameters in the European Arctic during the Year of Polar Prediction Special Observing Period Northern Hemisphere 1,  
 1082 Weather Forecast, 34, 959–983, https://doi.org/10.1175/WAF-D-19-0003.1, 2019.

1083 Köhler, M., Ahlgrimm, M. and Beljaars, A. (2011). Unified treatment of dry convective and stratocumulus topped boundary  
 1084 layers in the ECMWF model. *Q. J. R. Meteorol. Soc.*, 137, 43–57.

1085 Lawrence, H., Bormann, N., Sandu, I., Day, J., Farnan, J., and Bauer, P.: Use and impact of Arctic observations in the ECMWF  
 1086 Numerical Weather Prediction system. *Q. J. R. Meteorol. Soc.*, 145, 3432–3454, https://doi.org/10.1002/qj.3628, 2019.

1087 Lenderink, G. and Holtslag, A.A.M. (2004), An updated length-scale formulation for turbulent mixing in clear and cloudy  
 1088 boundary layers. *Q.J.R. Meteorol. Soc.*, 130: 3405–3427. https://doi.org/10.1256/qj.03.117

1089 Li, J. and H.W Barker, 2005: A radiation algorithm with correlated-k distribution. Part I: Local thermal equilibrium. *J. Atmos.  
 1090 Sci.*, 62, 286–309.

1091 Lott, F. and Miller, M. J. (1997). A new subgrid-scale orographic drag parametrization: Its formulation and testing. *Q. J. R.  
 1092 Meteorol. Soc.*, 123, 101–127.

1093 Louis, J. F.: A parametric model of vertical eddy fluxes in the atmosphere | SpringerLink, *Bound.-Layer Meteorol.*, 1979.

1094 Masson, V., Le Moigne, P., Martin, E., Faroux, S., Alias, A., Alkama, R., Belamari, S., Barbu, A., Boone, A., Bouyssel, F.,  
 1095 Brousseau, P., Brun, E., Calvet, J.-C., Carrer, D., Decharme, B., Delire, C., Donier, S., Essaouini, K., Gribelin, A.-L., Giordani,  
 1096 H., Habets, F., Jidane, M., Kerdraon, G., Kourzeneva, E., Lafayse, M., Lafont, S., Lebeaupin Brossier, C., Lemonsu, A.,  
 1097 Mahfouf, J.-F., Marguinaud, P., Mokhtari, M., Morin, S., Pigeon, G., Salgado, R., Seity, Y., Taillefer, F., Tanguy, G., Tulet,  
 1098 P., Vincendon, B., Vionnet, V., and Volodko, A.: The SURFEXv7.2 land and ocean surface platform for coupled or offline  
 1099 simulation of earth surface variables and fluxes, *Geosci. Model Dev.*, 6, 929–960, https://doi.org/10.5194/gmd-6-929-2013,  
 1100 2013.

1101 Milbrandt, J. A. and Morrison, H.: Parameterization of Cloud Microphysics Based on the Prediction of Bulk Ice Particle  
 1102 Properties. Part III: Introduction of Multiple Free Categories, *J. Atmospheric Sci.*, 73, 975–995, https://doi.org/10.1175/JAS-  
 1103 D-15-0204.1, 2016.

1104 Milbrandt, J. A., Bélair, S., Faucher, M., Vallée, M., Carrera, M. L., and Glazer, A.: The Pan-Canadian High Resolution (2.5  
 1105 km) Deterministic Prediction System, *Weather Forecast.*, 31, 1791–1816, https://doi.org/10.1175/WAF-D-16-0035.1, 2016.

1106 Miller, N. B., Shupe, M. D., Lenaerts, J. T. M., Kay, J. E., de Boer, G., & Bennartz, R. (2018). Process-based model evaluation  
 1107 using surface energy budget observations in central Greenland. *Journal of Geophysical Research: Atmospheres*, 123, 4777–  
 1108 4796. https://doi.org/10.1029/2017JD027377

1109 Mlawer, E. J., Taubman, S. J., Brown, P. D., Iacono, M. J. and Clough, S. A. (1997). Radiative transfer for inhomogeneous  
 1110 atmospheres: RRTM, a validated correlated-k model for the longwave. *J. Geophys. Res.*, 102D, 16663–16682.

1111 Mariani, Z., Morris, S., Uttal, T., Akish, E., Crawford, R., Huang, L., Day, J., Tjernström, J., Godøy, Ø., Ferrighi, L., Hartten,  
 1112 L., Holt, J., Cox, C., O'Connor, E., Pirazzini, R., Maturilli, M., Prakash, G., Mather, J., Strong, K., Fogal, P., Kustov, V.,  
 1113 Svensson, G., Gallagher, M., and Vasel, B.: Special Observing Period (SOP) Data for the Year of Polar Prediction site Model  
 1114 Intercomparison Project (YOPPSiteMIP), *Earth Syst. Sci. Data Discuss. [preprint]*, https://doi.org/10.5194/essd-2023-497, in  
 1115 review, 2024.

1116 Morrison, H. and Milbrandt, J. A.: Parameterization of Cloud Microphysics Based on the Prediction of Bulk Ice Particle  
 1117 Properties. Part I: Scheme Description and Idealized Tests, *J. Atmospheric Sci.*, 72, 287–311, https://doi.org/10.1175/JAS-D-  
 1118 14-0065.1, 2015.

**Deleted:** Miller, N. B., Shupe, M. D., Cox, C. J., Noone, D., Persson, P. O. G., and Steffen, K.: Surface energy budget responses to radiative forcing at Summit, Greenland, *The Cryosphere*, 11, 497–516, https://doi.org/10.5194/tc-11-497-2017, 2017.

**Deleted:** 1

**Deleted:** Morris et al. (submitted to ESSD): Special Observing Period (SOP) Data for the Year of Polar Prediction site Model Intercomparison Project (YOPPSiteMIP)

1127 Morrison, H., Milbrandt, J. A., Bryan, G. H., Ikeda, K., Tessendorf, S. A., and Thompson, G.: Parameterization of Cloud  
 1128 Microphysics Based on the Prediction of Bulk Ice Particle Properties. Part II: Case Study Comparisons with Observations and  
 1129 Other Schemes, *J. Atmospheric Sci.*, 72, 312–339, <https://doi.org/10.1175/JAS-D-14-0066.1>, 2015.

1130 Müller, M., and Coauthors, 2017: AROME-MetCoOp: A Nordic Convective-Scale Operational Weather Prediction Model.  
 1131 *Wea. Forecasting*, 32, 609–627, <https://doi.org/10.1175/WAF-D-16-0099.1>.

1132 Noilhan, J., & Planton, S. (1989). A Simple Parameterization of Land Surface Processes for Meteorological Models, *Monthly  
 1133 Weather Review*, 117(3), 536-549.

1134 O'Connor, E. (2023). Merged observation data file for Sodankyla. Norwegian Meteorological Institute.  
 1135 <https://doi.org/10.21343/M16P-PQ17>

1136 Pailleux, J., Geleyn, J.-F., Hamrud, M., Courtier, P., Thépaut, J.-N., Rabier, F., Andersson, E., Burridge, D., Simmons, A.,  
 1137 Salmond, D., Khatib, E., and Fischer, C.: Twenty-five years of IFS/ARPEGE, <https://doi.org/10.21957/FTU6MFVY>, 2014.

1138

1139 Pergaud, J., Masson, V., Malardel, S. et al. A Parameterization of Dry Thermals and Shallow Cumuli for Mesoscale Numerical  
 1140 Weather Prediction. *Boundary-Layer Meteorol* 132, 83–106 (2009). <https://doi.org/10.1007/s10546-009-9388-0>

1141

1142 Pinty, J.-P. and P. Jabouille (1998), A mixed-phase cloud parameterization for use in a mesoscale non-hydrostatic model:  
 1143 Simulations of a squall line and of orographic precipitation, *Proc. Conf. on Cloud Physics*, 217–220.

1144

1145 Pithan, F., Medeiros, B., and Mauritsen, T.: Mixed-phase clouds cause climate model biases in Arctic wintertime temperature  
 1146 inversions, *Clim. Dyn.*, 43, 289–303, <https://doi.org/10.1007/s00382-013-1964-9>, 2014.

1147 Pithan, F., Ackerman, A., Angevine, W. M., Hartung, K., Ickes, L., Kelley, M., Medeiros, B., Sandu, I., Steeneveld, G.-J.,  
 1148 Sterk, H. a. M., Svensson, G., Vaillancourt, P. A., and Zadra, A.: Select strengths and biases of models in representing the  
 1149 Arctic winter boundary layer over sea ice: the Lareform 1 single column model intercomparison, *J. Adv. Model. Earth Syst.*,  
 1150 8, 1345–1357, <https://doi.org/10.1002/2016MS000630>, 2016.

1151 Prill, F., Reinert, D., Rieger, D., Zängl, G.: ICON Tutorial - Working with the ICON model,  
 1152 [https://doi.org/10.5676/dwd\\_pub/nwv/icon\\_tutorial2020](https://doi.org/10.5676/dwd_pub/nwv/icon_tutorial2020), 2020

1153 Raschendorfer, M., 2001: The new turbulence parameterization of LM. *COSMO Newslett.*, 1, 89–97.

1154 Remes, T. (2023). MMDFs for the MetNorway AROME regional forecast model for various Arctic sites. Norwegian  
 1155 Meteorological Institute. <https://doi.org/10.21343/47AX-MY36>

1156 Rodwell, M. J. and Palmer, T. N.: Using numerical weather prediction to assess climate models, *Q. J. R. Meteorol. Soc.*, 133,  
 1157 129–146, <https://doi.org/10.1002/qj.23>, 2007.

1158 Sandu, I., Beljars, A., Bechtold, P., Mauritsen, T., and Balsamo, G.: Why is it so difficult to represent stably stratified  
 1159 conditions in numerical weather prediction (NWP) models?, *J. Adv. Model. Earth Syst.*, 5, 117–133,  
 1160 <https://doi.org/10.1002/jame.20013>, 2013.

1161 Sedlar, J., Tjernström, M., Rinke, A., Orr, A., Cassano, J., Fettweis, X., et al. (2020). Confronting Arctic troposphere, clouds,  
 1162 and surface energy budget representations in regional climate models with observations. *Journal of Geophysical Research:  
 1163 Atmospheres*, 125. <https://doi.org/10.1029/2019JD031783>

1164 Seity, Y., Brousseau, P., Malardel, S., Hello, G., Bénard, P., Boutilier, F., Lac, C., and Masson, V.: The AROME-France  
 1165 Convective-Scale Operational Model, *Mon. Weather Rev.*, 139, 976–991, <https://doi.org/10.1175/2010MWR3425.1>, 2011.

1166 Seifert, A.: A revised cloud microphysical parameterization for COSMO-LME. *COSMO News Letter No. 7*,  
 1167 <http://www.cosmo-model.org>, 2008

1168 Seity, Y., Lac, C., Bouyssel, F., Riette, S., & Boutilier, Y. (2012, November). Cloud and microphysical schemes in ARPEGE  
 1169 and AROME models. In *Proceedings of the Workshop on Parametrization of Clouds and Precipitation (ECMWF)*, Reading,  
 1170 UK (pp. 5-8).

**Deleted:** Roehrig, R., Beau, I., Saint-Martin, D., Alias, A., Decharme, B., Guérémy, J.-F., Voldoire, A., Abdel-Lathif, A. Y., Bazile, E., Belamari, S., Blein, S., Bouniol, D., Boutilier, Y., Cattiaux, J., Chauvin, F., Chevallier, M., Colin, J., Douville, H., Marquet, P., Michou, M., Nabat, P., Oudar, T., Peyrille, P., Piriou, J.-M., Salas y Melia, D., Séférian, R., and Sénési, S.: The CNRM Global Atmosphere Model ARPEGE-Climat 6.3: Description and Evaluation, *J. Adv. Model. Earth Syst.*, 12, e2020MS002075, <https://doi.org/10.1029/2020MS002075>, 2020.

**Deleted:** 1

1181 Solomon, A., Shupe, M.D., Svensson, G., Barton, N.P., Batrak, Y., Bazile, E., Day, J.J., Doyle, J.D., Frank, H.P., Keeley, S.,  
 1182 Remes, T., and Tolstykh, M., 2023. The Winter Central Arctic Surface Energy Budget; A Model Evaluation using Observations  
 1183 from the MOSAiC Campaign. *Elem Sci Anth*, in press.

1184 Soares, P., P. Miranda, A. Siebesma, and J. Teixeira, 2004: An eddy-diffusivity/mass-flux parametrization for dry and shallow  
 1185 cumulus convection. *Quart. J. Roy. Meteor. Soc.*, 130, 33653383, doi:10.1256/qj.03.223.

1186 Siebesma, A. P., P. M. Soares, and J. Teixeira, 2007: A combined eddy diffusivity mass-flux approach for the convective  
 1187 boundary layer. *J. Atmos. Sci.*, 64, 1230–1248, doi:10.1175/JAS3888.1.

1188 Svensson, G. and Karlsson, J.: On the Arctic Wintertime Climate in Global Climate Models, *J. Clim.*, 24, 5757–5771,  
 1189 <https://doi.org/10.1175/2011JCLI4012.1>, 2011.

1190 Tarasova, T. A., and B. A. Fomin, 2007: The Use of New Parameterizations for Gaseous Absorption in the CLIRAD-SW Solar  
 1191 Radiation Code for Models. *J. Atmos. Oceanic Technol.*, 24, 1157–1162, <https://doi.org/10.1175/JTECH2023.1>.

1192 Tiedtke, M., 1993: Representation of Clouds in Large-Scale Models. *Monthly Weather Review*, 121 (11), 3040–3061,

1193 Tjernström, M., Žagar, M., Svensson, G., Cassano, J. J., Pfeifer, S., Rinke, A., Wyser, K., Dethloff, K., Jones, C., Semmler,  
 1194 T., and Shaw, M.: ‘Modelling the Arctic Boundary Layer: An Evaluation of Six Arcmip Regional-Scale Models using Data  
 1195 from the Sheba Project,’ *Bound.-Layer Meteorol.*, 117, 337–381, <https://doi.org/10.1007/s10546-004-7954-z>, 2005.

1196 Tjernström, M., Svensson, G., Magnusson, L., Brooks, I. M., Prytherch, J., Vüllers, J., and Young, G.: Central Arctic weather  
 1197 forecasting: Confronting the ECMWF IFS with observations from the Arctic Ocean 2018 expedition, *Q. J. R. Meteorol. Soc.*,  
 1198 147, 1278–1299, <https://doi.org/10.1002/qj.3971>, 2021.

1199 Tolstykh, M. (2023). MMDFs for the Roshydromet-SLAV global forecast model for various Arctic sites. Norwegian  
 1200 Meteorological Institute. <https://doi.org/10.21343/J4SJ-4N61>

1201 Tolstykh, M., Shashkin, V., Fadeev, R., and Goyman, G.: *Vorticity-divergence semi-Lagrangian global atmospheric model*–  
 1202 *SL-AV20: dynamical core*. *Geosci. Model Dev.*, 10, 1961–1983, <https://doi.org/10.5194/gmd-10-1961-2017>, 2017.

1203 Tolstykh, M. A., Fadeev, R. Yu., Shashkin, V. V., Goyman, G. S., Zaripov, R. B., Kiktev, D. B., Makhnorylova, S. V., Mizyak,  
 1204 V. G., and Rogutov, V. S.: Multiscale Global Atmosphere Model SLAV: The Results of Medium-range Weather Forecasts,  
 1205 Russ. Meteorol. Hydrol., 43, 773–779, <https://doi.org/10.3103/S1068373918110080>, 2018.

1206 Uttal, T., Starkweather, S., Drummond, J. R., Vihma, T., Makshtas, A. P., Darby, L. S., Burkhardt, J. F., Cox, C. J., Schmeisser,  
 1207 L. N., Haiden, T., Maturilli, M., Shupe, M. D., De Boer, G., Saha, A., Grachev, A. A., Crepinsek, S. M., Bruhwiler, L.,  
 1208 Goodison, B., McArthur, B., Walden, V. P., Dlugokencky, E. J., Persson, P. O. G., Lesins, G., Laurila, T., Ogren, J. A., Stone,  
 1209 R., Long, C. N., Sharma, S., Massling, A., Turner, D. D., Stanitski, D. M., Asmi, E., Aurela, M., Skov, H., Eleftheriadis, K.,  
 1210 Virkkula, A., Platt, A., Forland, E. J., Iijima, Y., Nielsen, I. E., Bergin, M. H., Candlish, L., Zimov, N. S., Zimov, S. A.,  
 1211 O’Neill, N. T., Fogal, P. F., Kivi, R., Konopleva-Akish, E. A., Verlinde, J., Kustov, V. Y., Vasel, B., Ivakhov, V. M., Viisanen,  
 1212 Y., and Intriери, J. M.: International Arctic Systems for Observing the Atmosphere: An International Polar Year Legacy  
 1213 Consortium, *Bull. Am. Meteorol. Soc.*, 97, 1033–1056, <https://doi.org/10.1175/BAMS-D-14-00145.1>, 2015.

1214 Uttal, T., Hartten, L. M., Khalsa, S. J., Casati, B., Svensson, G., Day, J., Holt, J., Akish, E., Morris, S., O’Connor, E., Pirazzini,  
 1215 R., Huang, L. X., Crawford, R., Mariani, Z., Godoy, Ø., Tjernström, J. A. K., Prakash, G., Hickmon, N., Maturilli, M., and  
 1216 Cox, C. J.: *Merged Observatory Data Files (MODFs): An Integrated Observational Data Product Supporting Process-Oriented*  
 1217 *Investigations and Diagnostics, EGUSphere [preprint]*, <https://doi.org/10.5194/egusphere-2023-2413>, 2023.

1218

1219 Van de Wiel, B. J. H., Vignon, E., Baas, P., van Hooijdonk, I. G. S., van der Linden, S. J. A., Antoon van Hooft, J., Bosveld,  
 1220 F. C., de Roode, S. R., Moene, A. F., & Genthon, C. (2017). Regime Transitions in Near-Surface Temperature Inversions: A  
 1221 Conceptual Model, *Journal of the Atmospheric Sciences*, 74(4), 1057-1073. doi: <https://doi.org/10.1175/JAS-D-16-0180.1>

1222 van Meijgaard, E., L. van Ulft, G. Lenderink, S. De Roode, E. L. Wipfler, R. Boers, and R. van Timmermans, 2012: Refinement  
 1223 and application of a regional atmospheric model for climate scenario calculations of Western Europe. *KVR Research Rep.*  
 1224 054/12, 44 pp. [Available online at <http://library.wur.nl/> WebQuery/wurpubs/fulltext/312258.]

1225 Wallace, J. M., Tibaldi, S., & Simmons, A. J. (1983). Reduction of systematic forecast errors in the ECMWF model through  
 1226 the introduction of an envelope orography. *Quarterly Journal of the Royal Meteorological Society*, 109(462), 683–717.  
 1227 <https://doi.org/10.1002/qj.49710946202>

**Deleted:** Seifert, A.: A revised cloud microphysical parameterization for COSMO-LME. *COSMO News Letter No. 7*, <http://www.cosmo-model.org>, 2008

**Deleted:** 1

**Deleted:** Shupe, M.D., Rex, M., Blomquist, B., Persson, P.O.G., Schmale, J., Uttal, T., Althausen, D., Angot, H., Archer, S., Barateau, L. and Beck, I., 2022. Overview of the MOSAiC expedition: Atmosphere. *Elem Sci Anth*, 10(1), p.00060.

**Deleted:** 1

**Formatted:** Space After: 0 pt, Line spacing: 1.5 lines

**Deleted:** Uttal, T. L.M. Hartten, S.J. Khalsa, B. Casati, G. Svensson, J. Day, M. Gallagher, J. Holt, E. Aksh, S. Morris, E. O’Connor, R. Pirazzini, L. Huang, R. Crawford, Z. Mariani, O. Godoy, J. A.K. Tjernstrom, G. Prakesh, N. Hickmon, M. Maturilli, and C. Cox, *Merged Observatory Data Files (MODFs): An Integrated Research Data Product Supporting Process Oriented Investigations and Diagnostics*. 2023.

**Formatted:** Line spacing: Multiple 1.15 li

1244 Wilkinson, M., Dumontier, M., Aalbersberg, I. et al. The FAIR Guiding Principles for scientific data management and  
1245 stewardship. *Sci Data* 3, 160018 (2016). <https://doi.org/10.1038/sdata.2016.18>

1246 Zängl, G., Reinert, D., Rípodas, P., and Baldauf, M.: The ICON (ICOsaHedral Non-hydrostatic) modelling framework of DWD  
1247 and MPI-M: Description of the non-hydrostatic dynamical core, *Q. J. R. Meteorol. Soc.*, 141, 563–579,  
1248 <https://doi.org/10.1002/qj.2378>, 2015.

1249  
1250  
1251  
1252

**Deleted:** Wexler, H.: Cooling in the lower atmosphere and the  
structure of polar continental air. *Mon. Weather Rev.*, 64, 122–136,  
[https://doi.org/10.1175/1520-0493\(1936\)64<122:CITLAA>2.0.CO;2](https://doi.org/10.1175/1520-0493(1936)64<122:CITLAA>2.0.CO;2), 1936.

**Deleted:** 1